8-1-2018

Fixed Bed Reactor Design for Thermochemical Energy Storage Using Ca(OH)2 /CaO

Qasim Ranjha
Lehigh University, qasim.engg@gmail.com

FIXED BED REACTOR DESIGN FOR THERMOCHEMICAL ENERGY STORAGE USING Ca(OH)2 /CaO

by

Qasim Ali Ranjha

A Dissertation

Presented to the Graduate and Research Committee

of Lehigh University

in Candidacy for the Degree of

Doctor of Philosophy

in

Mechanical Engineering

Lehigh University

(August 2018)

Approved and recommended for acceptance as a dissertation in partial fulfillment of the requirements for the degree of Doctor of Philosophy in Mechanical Engineering

Qasim Ali Ranjha

FIXED BED REACTOR DESIGN FOR THERMOCHEMICAL ENERGY STORAGE USING $Ca(OH)_2$ /CaO

_____

Defense Date

Dissertation Adviser

_____

Dr. Alparslan Oztekin

_____

Approved Date

Committee Members:

_____

Dr. Jacob Kazakia

_____

Dr. Edmund Webb

III

_____

Dr. Kai Landskron

ACKNOWLEDGMENTS

I am sincerely grateful to my advisor Dr. Alparslan Oztekin for his unconditional support and expert guidance at all stages during my Ph.D. Working under Dr. Oztekin's supervision made this long, and stressful at times, journey much easier for me. I am also thankful to my committee members Dr. Jacob Kazakia, Dr. Edmund Webb and Dr. Kai Landskron for their valuable feedback on my work. I also appreciate the wonderful company and the help from fellow Ph.D. students whenever I needed.

I am especially thankful to United States Educational Foundation in Pakistan, Institute of International Education in USA and Higher Education in Pakistan for the Fulbright scholarship for my entire Ph.D. program.

Finally, it is all due to the support and prayers of my parents, wife, kids and my siblings. They are the real blessings of my life.

TABLE OF CONTENTS

LIST OF TABLES

LIST OF FIGURES

ABSTRACT

Thermochemical energy storage (TCES) is an attractive mode of storing solar energy in the form of heat to be used with concentrated solar power (CSP) plants. Thermal energy is stored/released using a reverse endothermic/ exothermic reaction. TCES offers clear advantages over the other thermal energy storage (TES) options with sensible heat storage (SHS) and latent heat storage (LHS) in terms of energy density, storage time and the temperature range for the storage and release of the heat. However, this technique of storing the solar power at higher temperatures is still at laboratory or pilot scale, and researchers are trying to develop viable storage systems using potential candidate reaction systems for TCES. The reversible reaction system involving $CaO/Ca(OH)_2$ has great potentials to be used as TCES with certain advantages, in terms of cost, availability, industrial feedback, long-term storage and charge-discharge temperature range, over the other reaction systems. Despite these advantages, the reaction system suffers from drawbacks which include lower thermal conductivity of the solid reaction materials. In this study, various reactor configurations are investigated with particular regard to the heat transfer to and from the bed during charging and discharging processes respectively. A mathematical model is developed including reaction kinetics and energy and mass transport within the reaction bed and heat transfer fluid (HTF). The model is solved numerically using finite elements and is applied to simulate various possible reactor configurations with fixed reaction beds. A reactor with a rectangular reaction bed heated and cooled by flat plate heat exchanger is considered first. The model is validated against the available experiments for this reactor configuration, and parametric studies are performed involving bed porosity and HTF flow velocity. The

model is then applied to various other configurations with a circular reaction bed. Different heat exchanger designs for the circular reaction bed are studied and compared for various bed sizes and HTF flow conditions. Heat transfer enhancements (HTE) are introduced within the circular reaction bed to overcome the problem of lower thermal conductivity. It is found that the heat transfer within and to/from the reaction bed are important aspects in the design of any storage system, especially for the $CaO/Ca(OH)_2$ reaction system where the thermal conductivity of the storage material is low. A circular bed designed with the heat transfer enhancements and heated/cooled with air flowing perpendicular to the bed axis is the most efficient configuration in terms of power ratings and simplicity of the operation. This design also allows easy upscaling of the reactor by increasing the number of the reaction beds and their size. The findings from this study would be quite useful in designing and optimizing TCES based on $CaO/Ca(OH)_2$ or any other gas-solid reactions involving similar kinetics.

NOMENCLATURE

Acronyms		V	Molar density of solid reactant(s), $\frac{\rho_{rs}}{M_{rs}}$,mol/m^3
CSP	Concentrated Solar Power	v	Volume of reaction bed, m^3
HTE	Heat transfer enhancements	X	Conversion
HTF	Heat Transfer Fluid	***Greek Symbols***	
TES	Thermal Energy Storage	$\mathcal{K}$	Reaction rate constant, 1/sec
TCES	Thermochemical energy storage	ϵ	Porosity
Full Scripts		η	Dynamic viscosity of steam, Pa-s
A	Pre-exponential factor, 1/s	μ	Dynamic viscosity of air, Pa-s
C	Specific heat, J/(kg.K)	λ	Thermal conductivity, W/m.K
D	Diameter	ρ	Density, kg/m^3
E	Activation energy, J/mole	***Subscripts***	
h	Height of reactor	b	Reaction bed
ΔH	Enthalpy of reaction, J/mol	c	Channel
K	Permeability	D	Dehydration
l	Characteristic length of HTF channel	eff	Effective
M	Molar mass, kg/mol	h	Hydraulic
P	Pressure, Pa	H	Hydration
r	Radius	eq	Equilibrium
R	Gas constant, J / mol. K	ini	Initial
$\dot{R}$	Rate of reaction	M	Mass
Re	Reynolds number	Q	Heat
$\dot{S}_Q$	Heat source/sink, W/m^3	r	Reactor
$\dot{S}_m$	Mass source/sink, kg/ (m^3. S)	rs	Reactant solid
T	Temperature, K	S	Solid phase/reaction bed
t	Time, sec	st	Steam
t	Thickness		
u	Velocity of the gaseous phase, m/s		
U	Velocity of air		

CHAPTER 1 INTRODUCTION

1.1 Background and Motivation

With increasing awareness of climate change and harms to our ecosystem by the use of fossil fuels, the emphases on the use of alternate, clean and renewable energy resources have increased in the past few decades. Solar energy, being one of the largest renewable energy resources, is exploited to generate electricity directly and indirectly using photovoltaics (PV) and concentrated solar power (CSP) plants respectively. Like most other renewable energy resources, the problem with this abundant energy resource is that it is intermittent because of the weather fluctuations, changing seasons and day-night cycles. The solution to this problem, in the case of CSP plants, is high-temperature thermal energy storage (TES) systems. TES can help overcome the intermittent nature of the solar irradiance by daily, weekly or seasonal balance of demand and supply of the energy. Proper implantation of TES will not only improve the efficiency of the solar systems but will also increase the renewable energy share in the total energy.

A TES system is described in terms of storage capacity, power rating, storage period, efficiency and cost. The storage capacity is determined by the properties of the storage medium, the technique to store energy and the size of the storage system. The power is measured in terms of the rate of charging and discharging. Solar energy can be stored in three forms of the thermal energy namely sensible heat, latent heat and thermochemical energy. Accordingly, the potential storage materials are classified based on these three techniques of TES.

TES systems based on sensible heat storage are being widely used in low-temperature commercial applications [1]. Despite being simplest of the three techniques, the sensible heat storage cannot be used for high-temperature applications due to low energy densities of storage materials and thermal losses during storage period [2,3]. Latent heat storage materials have higher energy densities than the sensible energy storage materials but can only be used for low to medium temperature application [4-5] in addition to problem of heat losses during the storage period. Also, due to instability and complexity of the phase change process [6,7], latent heat storage systems are still at pilot scale. Third possibility, the thermochemical energy storage (TCES), is more advantageous in terms of energy density and storage options [8-10]. Thermochemical storage materials have almost ten times the energy density of phase change materials [8], can be stored over long periods of time and can be transported to long distances in ambient conditions without thermal losses. Despite these advantages over the sensible and latent heat storages, TCES systems are still under laboratory research to overcome challenges in using them as full-scale TES [9-10]. One of the challenges is proper reactor design in terms of heat exchange between the reaction material and the heat transfer fluid. In this study, various possible configurations of fixed bed reactor are considered and investigated. The results obtained would be helpful in choosing the proper configuration with respect to heat transfer to and from the reaction bed. In addition, heat transfer enhancements are incorporated in the selected configuration to overcome a common drawback of low thermal conductivity of the TCES materials.

1.2 State of the Art

TCES systems are based on either sorption or chemical reaction [11-12]. Both sorption and chemical reaction systems rely on a reversible reaction where the forward reaction is endothermic for heat storage and the reverse reaction is exothermic for heat release. Sorption mechanisms involve adsorption/desorption of gas or vapor over the surface of a solid or in a liquid. Sorption systems, in general, generate a low amount of energy and are, therefore, only suited to low-temperature applications [13-18]. The second class of TCES systems are usually decomposition and synthesis type reactions and can be used for a temperature range (300^0C-1000^0C) suitable for high-temperature solar applications [19-21]. Chemical reaction systems studied for TES applications are classified as metallic hydrides, carbonate systems, hydroxide systems, REDOX (oxidation-reduction) systems, and ammonia systems[8,19,21,22]. According to the criteria laid down by Wentworth et al [23] and later updated by Pardo et al [8], the selection of the reaction system depends on a number of factors including, but not limited to, temperature range for exothermic and endothermic reactions, reaction enthalpies, volumetric or mass-energy densities, reversibility, rates of forward/reverse reaction, storage of reaction materials, experimental feedback, thermal conductivity, and cost.

Several investigators have reviewed the use of these reaction systems employed as TCES [8,11,20]. These studies provide a good understanding of each reaction system as to what extent it meets above selection criteria. A common drawback of metal hydride and carbonate systems is the storage of hydrogen and carbon dioxide which not only adds to the storage cost of the reactants/product but also makes their transportation, if needed, difficult [8,24,25,26]. REDOX reaction systems, on the other hand, involve costly and

toxic products in addition to the oxygen storage issue. These systems are least studied reactions for TCES applications, and their reaction kinetics are not well established [8,27,28]. TCES based on ammonia have been studied extensively at Australian National University (ANU) from late 90's to date, and successful integration to solar dish concentrators has been demonstrated [2,29,30]. However, storage of nitrogen and hydrogen, high operating pressure (100-200 bar), use of catalysts and incomplete conversion of both forward and reverse reactions make ammonia systems too challenging to be used for large-scale energy storage applications [8]. Hydroxide systems involve inexpensive and easily commercially available materials. Reactants and products in these reactions are non-toxic, do not require catalysts and have rather good reversibility [8,31-33]. Mg(OH)2/MgO pair and Ca(OH)2/CaO pair are two promising hydroxide systems studied extensively, and have over ten years of experimental feedbacks [8]. Reversible reactions for these systems are given as.

$$Ca(OH)_2\,(s) + \Delta H \leftrightarrow CaO(s) + H_2O(g) \qquad \Delta H = 104\ kJ/mol \qquad (1)$$

$$Mg(OH)_2\,(s) + \Delta H \leftrightarrow MgO(s) + H_2\,O(g) \qquad \Delta H = 81\ kJ/mol \qquad (2)$$

Guy Ervin [34] reported preliminary experimental findings on above two systems and concluded that $Ca(OH)_2$/CaO system is more suitable compared to $Mg(OH)_2$/MgO system based on materials cost, cycling stability, energy density and temperature range for the hydration and the dehydration reactions. In gas-solid reaction shown in equation 1, the temperature at which the exothermic reaction occurs is directly related to the steam pressure. Thus, the outlet temperature in the energy retrieval process can be easily set at a value within a desired temperature range by controlling the steam pressure.

Reaction beds for gas-solid reactions like the one presented in equation (1) can be either fixed (cylindrical or rectangular packed beds) or moving (rotary kilns or fluidized beds) [35,36]. Owing to higher complexity and cost of moving beds, studies investigating moving beds for high-temperature energy storage are very rare [36-38].

Design of fixed bed reactor for gas-solid exothermic/endothermic reactions depends on the mode of heat transfer (direct or indirect) and supply/removal of the reaction gas. S. Fujimoto et al. [39] investigated $Ca(OH)_2$/CaO system for heat pump applications. Two separate circular bed reactors were used for hydration and dehydration equipped with cooling coils and electric resistance heaters respectively. Michito Kanamori et al. [40] conducted lab-scale experiments to study hydration and dehydration process using circular packed beds. Cooling for the hydration was provided using an internal finned pipe running through the bed whereas heating for the dehydration was provided using electric heaters. H. Ogura et al. [41] studied the similar system numerically and experimentally for heat and mass transport within the particle bed. In an earlier study Fuji et al. [42] considered $Ca(OH)_2$/CaO reversible reaction for the storage and the retrieval of thermal energy. The reaction material was packed in spiral fins with a pitch of 3-5mm which were heated and cooled by air in the charging and the discharging process, respectively. M.N. Azpiazu et al. [43] investigated experimentally a rectangular packed bed heated and cooled by an anti-freeze solution and inserting fins within the bed for the enhancement of the heat transfer.

All of these studies dealt with indirect heating/cooling of the beds which results in low heat transfer due to the poor thermal conductivity of the reaction materials. One way to overcome this problem is to use heat transfer enhancements in reactor or heat

exchanger. H. Ogura et al. reported significant improvement in the heat storage and release by increasing the size of the heat exchanger [44] or by introducing fins into the reaction bed [45]. F. Schaube et al. [46,47] used direct heat transfer approach to enhance the heat transfer in which HTF and the reaction gas were forced through the porous bed simultaneously. In a similar approach, Pardo et al. [35,38] used fluidize reaction bed for $Ca(OH)_2/CaO$ system. The authors reported high-pressure drops in addition to required pumping work as major drawbacks of this approach.

Few recent studies focused on a rectangular shaped bed with indirect heat transfer. P. Schmidt et al. [48] designed and developed a pilot plant scale reactor with a plate heat exchanger to investigate $Ca(OH)_2/CaO$ system where the reaction gas and HTF were transported in a cross flow scheme. A two-dimensional transient model was also developed to be validated against experimental results. M. Schmidt et al. [49] conducted experiments on the same test bench to study the effects of the mass flow rate of HTF on the hydration process. In another work [50] these authors investigated both the hydration and the dehydration process using the same test bench for the steam pressures up to 198kPa. Simulations were conducted using two-dimensional reactor. Cross flow configuration was approximated by either co-current or counter-current flow of the reaction gas and HTF assuming highly porous bed. Charging and discharging processed for lower steam pressures (10 kPa and 100 kPa respectively) were carried out in rectangular packed bed [51]. In another work, discharge mode at higher steam pressures (200-470 kPa) was demonstrated using the same packed bed [52]. J. Yan et al. [53] studied experimentally the circular packed bed wherein the Li-doped $Ca(OH)_2$ was used

for the charging process whereas pure CaO for used for the heat release process. The heat was supplied indirectly using electric heaters.

1.3 Objective

This study is aimed at designing a reactor with indirectly heated fixed reaction beds of circular and rectangular cross-sections. In an indirectly heated reaction bed, HTF could flow in co-current, counter-current or cross flow to the reaction gas as depicted in Figure1. All the configurations shown in the Figure 1 are simulated and compared in terms of heat transfer to/from the bed. Parametric studies are performed for various bed porosities, bed sizes, and HTF flow conditions. Two and three dimensional geometries are simulated with operating conditions compatible with the high-temperature CSP plants. The results are validated against available experimental data from the literature

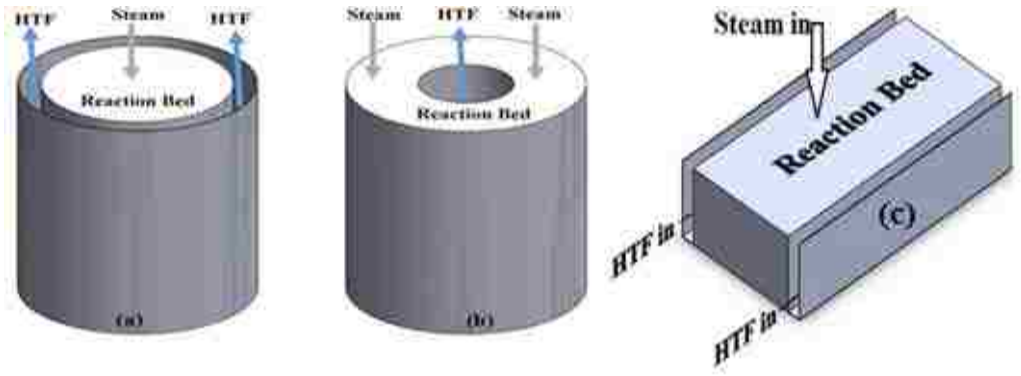

Figure 1. Reaction bed configurations with respect to flow of the reaction gas and the HTF. (a) Co-current flow, (b) counter-current flow, and (c) cross flow

CHAPTER 2 THE MODEL

The reactor configurations considered in this study consist of a fixed reaction bed heated and cooled indirectly by air as HTF through heat exchanger walls. The fixed reaction bed is filled with fine particles of solid reaction materials, $Ca(OH)_2$ and CaO, for charging and discharging processes respectively. Hence the reaction bed in this study refers to a porous domain, and the mathematical model is developed with energy and mass conservation equations for the reaction bed and the HTF. These equations are coupled to the reaction kinetics' equation and other auxiliary equations.

Following assumptions are applied in the model:

- The porous bed is treated as a continuum.
- The effective thermal conductivity of the bed is constant for a fixed value of the bed porosity.
- Interface condition is used at the wall between HTF and the bed.
- Heat transfer between the solid bed and the steam is neglected.
- Specific heat of the solids changes with temperature and bed density changes during the reaction.
- Steam is assumed to be saturated. Equilibrium temperature changes with the steam pressure. The equilibrium pressure and temperature are related by equation 25

2.1 Governing Equations

Following sections provide the details of the equations governing energy and mass transport within the reaction bed and HTF channel. Equations governing the reaction kinetics and the temperature dependence of various physical parameters are also given.

2.1.1 Mass and Energy Transport

Conservation of mass and energy equations are used for transport of the steam and heat within the porous bed. Mass balance for the steam is given as

$$\frac{\partial(\varepsilon.\rho_{st})}{\partial t} + \nabla(\rho_{st}.u_{st}) \pm \dot{S}_m = 0 \tag{3}$$

$$\dot{S}_{\mathbf{m}} = (1-\epsilon)\dot{R}M_{st} \tag{4}$$

where ε, ρ_{st} and u_{st} are bed porosity, steam density and steam velocity respectively. $\dot{S}_m$is the mass source/sink. The reaction rate,$\dot{R}$, is discussed in the next section. . Flow of the steam in the porous bed is governed by Darcy's law and Kozeny-Carman equation [48].

$$u_{st} = -\frac{\mathbf{K}}{\eta_{st}}\nabla P_{st} \tag{5}$$

$$\mathbf{K} = \frac{d_p^2.\varepsilon^3}{\Psi(1-\varepsilon)^2} \tag{6}$$

where P_{st} is the pressure of the steam, $\mathbf{K}$ is the bed permeability, η_{st} is the viscosity of the steam, and d_p is the diameter of solid particles. Ψ is called Carmen-

Kozeny (CK) factor and is measured empirically using pore shape factor and tortuosity. In this study Ψ =180 is used based on constant tortuosity and shape factor [48].

Energy balance equation for the porous bed is given as

$$(\rho C)_{eff}\frac{\partial(T_s)}{\partial t} + \rho_{st}C_{st}.u_{st}.\nabla T_s + \nabla.(-\lambda_{eff}.\nabla T_s) \pm \dot{S}_Q = 0 \quad (7)$$

$$\dot{S}_Q = (1-\epsilon)\dot{R}\Delta H \quad (8)$$

$$(\rho C)_{eff} = (1-\epsilon)(\rho C)_s + \epsilon(\rho C)_{st} \quad (9)$$

$$(\lambda)_{eff} = (1-\epsilon)\lambda_s + \epsilon\lambda_{st} \quad (10)$$

$$(\rho C)_s = (1-X)(\rho C)_{s1} + X(\rho C)_{s2} \quad (11)$$

where $\dot{S}_Q$ is the heat source/sink and ΔH is the enthalpy of the reaction. C, ρ, and λ are specific heat, density, and effective thermal conductivity, respectively. The subscripts st, s, s1 and s2 are used for properties of the steam, the bed, CaO and $Ca(OH)_2$. The terms with subscript eff represent the effective properties of the porous bed. Simple regression models from themophysical data of the solid materials [54,55] are used to determine the specific heat as a function of temperature for the temperature range of interest (300^0C-600^0C).

$$C_{p\,s1} = 0.1634\,\frac{J}{kg.°C^2}\,T + 844\,\frac{J}{kg.°C} \quad (12)$$

$$C_{p\,s2} = 0.3829\,\frac{J}{kg.°C^2}\,T + 1323.4\,\frac{J}{kg.°C} \quad (13)$$

HTF flow is laminar with the no-slip condition at walls. Accordingly, the effect of various parameters on the HTF outlet temperature is investigated. The energy equation for HTF is

$$(\rho C)_{HTF}\frac{\partial T_{HTF})}{\partial t} + (\rho C)_{HTF}.u_{HTF}.\nabla T_{HTF} + \nabla.(-\lambda_{HTF}.\nabla T_{HTF}) = 0 \qquad (14)$$

where T_{HTF} is the temperature of HTF and C_{HTF}, ρ_{HTF}, λ_{HTF} are the specific heat, the density and the thermal conductivity of HTF.

Continuity condition is applied at the interface between the reaction bed and the HTF channel in all cases except where heat transfer enhancements (HTE) were introduced. When HTE are introduced in the case of circular bed, the energy equation for the wall between the reaction bed and the HTF channel is also solved.

$$(\rho C)_{Wall}\frac{\partial T_{Wall})}{\partial t} + \nabla.(-\lambda_{Wall}.\nabla T_{Wall}) = 0 \qquad (15)$$

The subscript 'Wall' is for the wall between the reaction bed and HTF channel.

2.1.2 Reaction Kinetics

The rate of reaction, $\dot{R}$, in equation 4 and equation 8 is the rate at which reactants are converted into products. This rate is given by [56]

$$\dot{R} = V_{rs}\frac{dX}{dt} \qquad (16)$$

where V_{rs} is the molar density or the molar concentration of the reactant solid, X is the fraction of solid reactants converted into products during the hydration or the dehydration process.

The rate of conversion, $\frac{dX}{dt}$, is given by an equation of the form [57]

$$\frac{dX}{dt} = f(X)\mathcal{K}(T)h(P_{st}, P_{eq}) \text{ or } \quad t = g(X).\frac{1}{\mathcal{K}(T).h(P_{st}, P_{eq})} \tag{17}$$

$f(X)$ and $g(X)$ are functions of already converted material and depend on the material sample and experimental conditions for the hydration and the dehydration process. We utilize the n^{th} order reaction model [58,59] for $f(X)$and since the reaction in equation (1) is of the first order, it yields

$$f(X) = (1 - X) \quad \text{or} \quad g(X) = -\ln(1 - X) \tag{18}$$

$\mathcal{K}(T)$ in equation (17) is the temperature dependent reaction rate constant and is given by Arrhenius equation

$$\mathcal{K}(T) = Ae^{\left(\frac{-E}{RT}\right)} \tag{19}$$

where A is the pre-exponential factor, E is the activation energy, R is the gas constant and T is the reaction temperature.

$h(P_{st}, P_{eq})$ in equation (17) describes the pressure dependence and is a function of the water vapor pressure, P_{st}, and the reaction equilibrium pressure, P_{eq}

$$h(P_{st}, P_{eq}) = \mp\left(\frac{P_{st}}{P_{eq}} - 1\right)^{\alpha} \tag{20}$$

Positive and negative signs are for the hydration and the dehydration, respectively. Values of α is empirically determined for a material sample, and different values have been reported by different investigators. The value of α = 1 as reported by H. Ogura et al. [41] is employed here. Equations (17-19) yield a general form of the equation (16) to be used in this study as

$$\frac{dX}{dt} = \mp(1 - X).A.e^{\left(\frac{-E}{RT}\right)}\left(\frac{P}{P_{eq}} - 1\right) \quad (21)$$

In reversible reactions, an equilibrium state is when the rate of the forward reaction becomes equal to the rate of the reverse reaction. An equilibrium constant, $\mathbb{K}$, is used to determine the direction of reversible reactions. Given the enthalpy and the entropy of a reaction at standard conditions, $\mathbb{K}$ is given in terms of the partial pressure of the gaseous components of the reaction. For the reaction described in equation (1) steam is the only gas involved, so the equilibrium constant for this reaction is given as

$$\mathbb{K} = \left(\frac{P_{st}}{P^{\theta}}\right) \quad (22)$$

P_{st} and P^{θ} are the steam pressure and the standard atmospheric pressure, respectively. The equilibrium constant of the reversible reaction is related to the temperature by Van't Hoff equation

$$\ln \mathbb{K} = -\frac{\Delta H^{\theta}}{RT} + \frac{\Delta S^{\theta}}{R} \quad (23)$$

ΔH^{θ} and ΔS^{θ} are the enthalpy and the entropy of the reaction at standard conditions of the temperature and the pressure. R is the gas constant and T is the absolute temperature. A relationship between the reaction temperature and the steam pressure is obtained by combining equation (22) and equation (23).

$$\ln\left(\frac{P_{st}}{P^{\theta}}\right) = -\frac{\Delta H^{\theta}}{RT} + \frac{\Delta S^{\theta}}{R} \quad (24)$$

Several investigators have determined the relationship given in equation (24) based on their experiments for a range of the steam partial pressure [57,60-62]. The relationship based on experiments of Schaube et al. [57] is used here.

$$\ln\left(\frac{P_{st}}{10^5}\right) = -\frac{12845}{T_{eq}} + 16.508 \tag{25}$$

where the temperature and the pressure are measured in Kelvin and Pascal, respectively. With the linear relationship between the pressure of the reaction gas and the reaction temperature as depicted in the equation (25), the last term in equation (21) can also be expressed in terms of the temperature.

$$\frac{dX}{dt} = \mp(1 - X).A.e^{\left(\frac{-E}{RT}\right)}\left(\frac{T_s}{T_{eq}} - 1\right) \tag{26}$$

Where T_s is temperature of the reaction bed.

2.2 Numerical Solution

Coupled set of equations (3)-(14), (25) and (26) are solved numerically using finite elements with standard COMSOL modules. Initial and boundary conditions for each reactor configuration are detailed along with the results in the following chapters. Mesh convergence analyses are performed for all the cases for both hydration and dehydration processes. Time convergence is obtained by using adaptive time steps. Mesh is each refined until the results were independent of the mesh density.

CHAPTER 3 RECTANGULAR REACTION BED WITH PLATE HEAT EXCHANGER

A packed bed reactor of the rectangular cross section is considered first for validation of the mathematical model. Flat plate type heat exchanger is used at both sides of the bed for heat transfer to and from the reaction bed. This configuration is selected as it has already been experimentally tested at lab scale and results are available for verification purposes [49]. The reactor configuration is shown in Figure 2. Physical and geometric parameters are listed in the Table 1. Initial simulations are carried out with a two-dimensional model for the sake of simplicity and ease of the computation. After performing parametric studies on the two-dimensional model it is revealed that two-dimensional approximation is not valid for low bed porosities. Hence, the model is applied to a complete three-dimensional geometry as well.

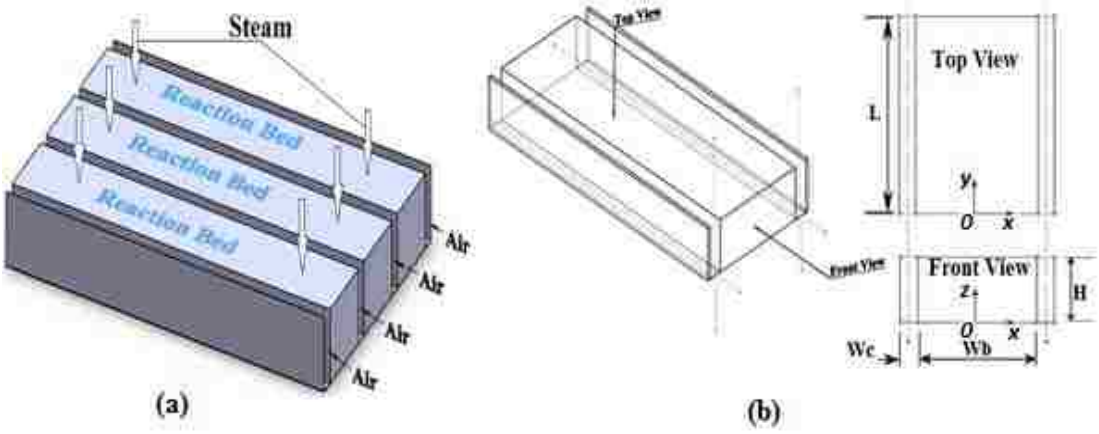

Figure 2. Arrangement of the reaction beds and HTF channels with flat plate heat exchanger (left) and a single bed with HTF channels on both sides as a computational domain (right). L and H are the length and width of the bed/HTF channel whereas Wb and Wc are the width of the bed and the HTF channel.

Table 1. Geometric and physical parameters of the reaction bed and HTF channel

Parameter	**Symbol**	**Value**
Real density CaO [47,57]	ρ_{s1}	1666 [g/cm^3]
Real density $Ca(OH)_2$ [47,57]	ρ_{s2}	2200 [g/cm^3]
Porosity [47]	ε	0.5-0.8
Solid particle size [50]	d_p	5 [μm]
Pre-exponential factor hydration [57]	A_H	53 x 10^3 [1/s]
Pre-exponential factor dehydration [57]	A_D	715 x 10^7 [1/s]
Activation energy hydration [57]	E_H	83 x 10^3 [J/mol]
Activation energy dehydration [57]	E_H	187 x 10^3[J/mol]
Effective thermal conductivity [57]	λ_{eff}	0.1-0.4 [W/(m.K)]
Width of the bed	Wb	20 [mm]
Width of the HTF channel	Wc	1.5 [mm]
Height of the bed	H	200 [mm]
Length of the bed	L	850 [mm]

3.1 Process Description

Charging (dehydration) process is carried out through forward endothermic decomposition of $Ca(OH)_2$ into CaO and steam. Heat energy is stored in the products as enthalpy of the reaction. The same energy is released in the reverse hydration of CaO in the discharging process. The description of these processes is given below. Initial and Boundary conditions are listed in the Table 2.

Table 2. Initial and boundary conditions.

Equation	Boundary/initial condition	Description
7,14	$T_s(x,y,z,t=0) = T_{HTF}(x,y,z,t=0) = T_{ini/H} = 350℃$	Initial temperature distribution; hydration
7,14	$T_s(x,y,z,t=0) = T_{HTF}(x,y,z,t=0) = T_{ini/D} = 450℃$	Initial temperature distribution; dehydration
7,14	$-n.\mathbf{q}(x,0,z,t) = -n.\mathbf{q}(x,L,z,t) = -n.\mathbf{q}(x,y,0,t)$ $= -n.\mathbf{q}(x,y,H,t) = 0 \quad \{\mathbf{q} = -\lambda\nabla T\}$	Insulated faces of the bed
7,14	$T_s\left(\pm\frac{Wb}{2},y,z,t\right) = T_{HTF}\left(\pm\frac{Wb}{2},y,z,t\right)$	Temperature continuity at the interface
14	$u_{HTF}\left(\pm\frac{Wb}{2},y,z,t\right) = 0$	No slip at the interface
3,5	$P(x,y,z,t=0) = 3000\ Pa \begin{cases} -\frac{Wb}{2} \le x \le \frac{Wb}{2} \\ 0 \le y \le L \\ 0 \le z \le H \end{cases}$ $P(x,y,H,t) = 198000\ Pa$	Initial pressure and steam pressure at top inlet; hydration
3,5	$P(x,y,z,t=0) = P(x,y,H,t) = 13300\ Pa$ $\begin{cases} -\frac{Wb}{2} \le x \le \frac{Wb}{2} \\ 0 \le y \le L \\ 0 \le z \le H \end{cases}$	Initial pressure and steam pressure at top outlet; dehydration
3,5	$-n.\rho u_{st}(x,0,z,t) = -n.\rho u_{st}(x,L,z,t)$ $= -n.\rho u_{st}(x,y,0,t)$ $= -n.\rho u_{st}\left(\pm\frac{Wb}{2},y,z,t\right) = 0$	No outflow of steam; hydration and dehydration

3.1.1 Charging (Dehydration) Process

The charging process is dehydration or thermal decomposition of $Ca(OH)_2$ into steam and CaO. At the beginning of dehydration, the bed and HTF are in thermal equilibrium, and the initial temperature is set equal to equilibrium temperature (450^0C) corresponding to the pressure of 20kPa.

The constant temperature of 590^0C is applied at the HTF inlet to keep its temperature well above the equilibrium temperature. Constant pressure equal to 20kPa is applied at the steam outlet boundary. Under this condition, the steam leaving the reactor will be condensed under ambient temperature. There is small pressure change inside the bed during the dehydration process due to initial and boundary conditions. Hence, a slight change in the equilibrium temperature is realized. High temperature of HTF permits an effective heat transfer from the HTF to the bed.

3.1.2 Discharging (Hydration) Process

In the discharging process the products of dehydration, the steam and CaO are brought together to form $Ca(OH)_2$ in an exothermic reaction. The heat release process commences by bringing both bed and the HTF in thermal equilibrium at 350^0C. This temperature corresponds to a pressure 3kPa according to equation (25). A constant pressure of 198kPa at the steam inlet is applied for which the equilibrium temperature is 550^0C. The HTF inlet temperature is kept constant while the solid temperature rises due to the heat released from the exothermic reaction. The equilibrium temperature changes as the pressure changes inside the bed according to equation (25).

3.2 Two-Dimensional Model

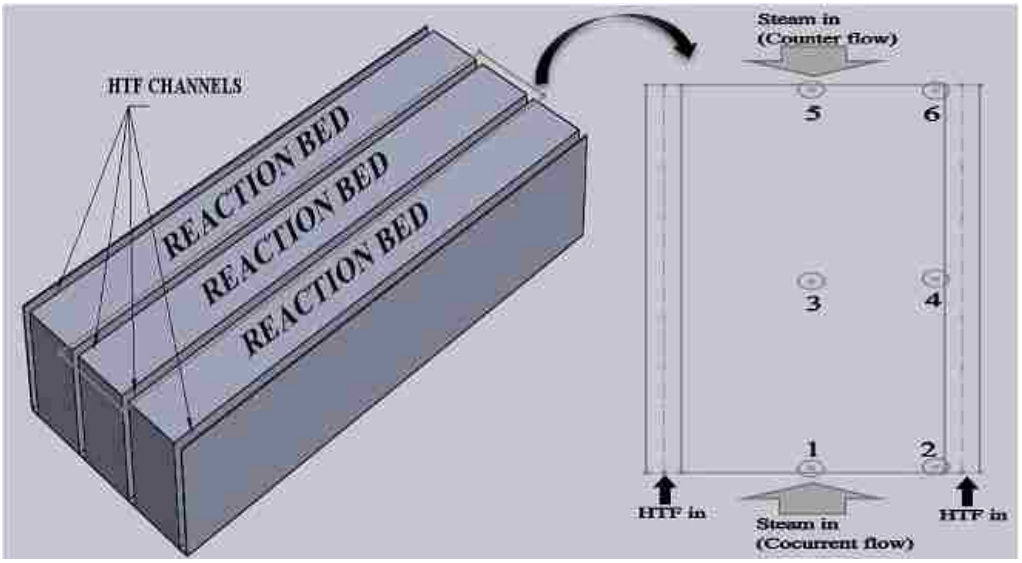

Figure 3. Reference geometry and two-dimensional model

Figure 3 shows the reactor and the two-dimensional domain for the simulation. Top surface of a single bed with HTF channels running along both sides is selected as a two-dimensional domain. The length of the bed (the height of the 2D model) is 850mm, and the width is 200mm. The width of HTF channel is 1.5mm. Steam enters the reaction bed from the top and HTF enters from the side as shown in Figure 2(a) in cross-flow configuration.

The cross-flow configuration cannot be modeled as a two-dimensional geometry. A two-dimensional model, however, yields a good prediction of the process if the length to height ratio of the bed is large and the bed porosity is sufficiently high so that the steam used in the reaction is immediately compensated. The top plane of the bed is chosen as the computational domain so that the contact length of HTF with the bed is not sacrificed with the 2D assumption. Initial and boundary conditions are taken from earlier

experimental studies [49] in order to validate the model. Symmetry condition is applied at the center line of each HTF channel. With the selected dimensions of HTF channel and HTF velocity, the flow inside the HTF channel is laminar.

3.2.1 Results-Charging and Discharging

Figure 4 and Figure 5 show the dehydration and hydration results respectively. These results correspond to a constant porosity of 0.8 and HTF inlet velocity of 25m/s. High porosity facilitates quick mass transfer and compensation of steam being consumed during hydration resulting in pressure equal to the equilibrium value throughout the bed immediately. The same conditions are realized for the dehydration process when the steam pressure increases due to the mass source but is quickly equilibrated owing to the high porosity of the bed.

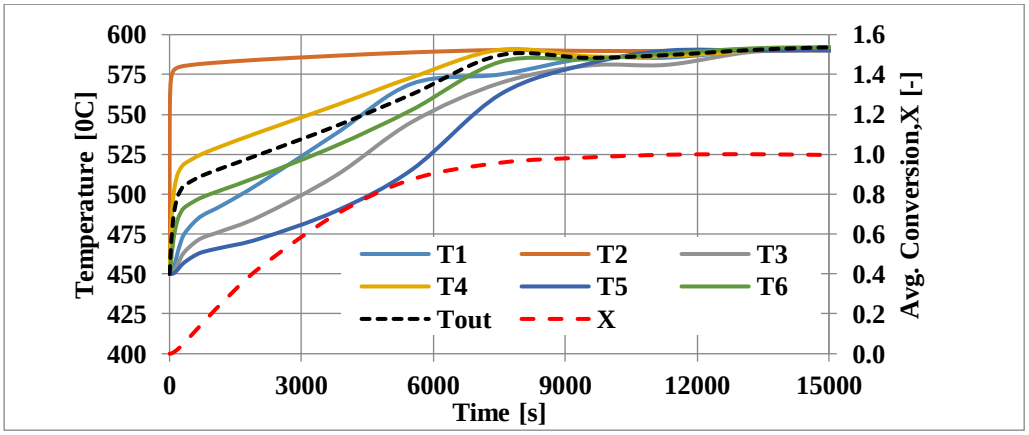

Figure 4. Bed temperatures during charging process (dehydration process), HTF average outlet temperature and average conversion. Bed temperatures are recorded at locations that are shown in Figure 3

During the hydration process, heat is generated as soon as the steam reaches all sections of the bed and the conversion proceeds with the heat transfer from the bed. During the dehydration, however, the heat transfer starts first followed by the conversion

and heat absorption. This results in different temperature gradients within the bed for hydration and dehydration with the same heat transfer conditions at the walls of the bed.

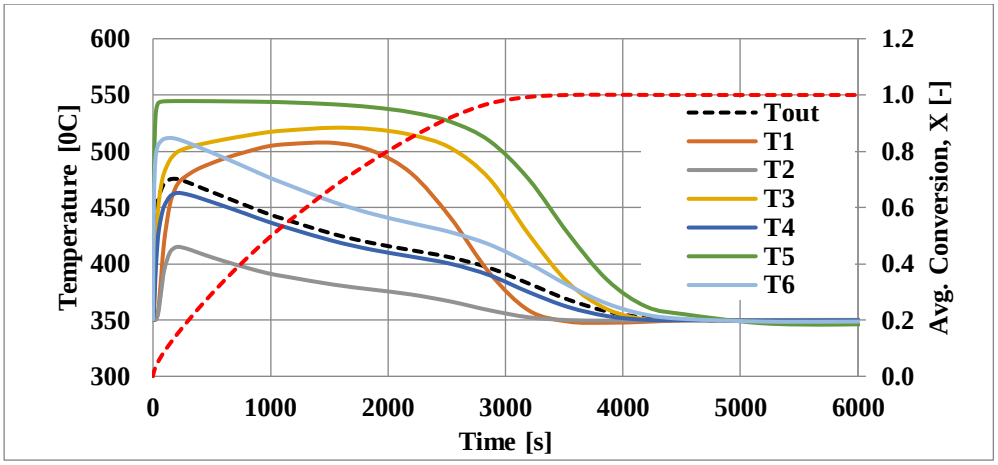

Figure 5. Bed temperatures during the discharging process (hydration process), HTF average outlet temperature and average conversion. Bed temperatures are recorded at locations that are shown in Figure 3.

3.2.2 Porosity Variations

The porosity of the bed may vary from 0.5 to 0.8 depending on how densely it is packed with the powder [23,25]. While high porosity aids in increasing the rate of mass transfer of the steam, it results in lower energy density and lower effective thermal conductivity. On the other hand, low porosity gives higher energy density and slightly better effective thermal conductivity but is accompanied by slow hydration due to limited mass transport. Figure 6 and Figure 7 show the reaction fronts at the beginning and a later stage of the hydration process for ε=0.8 and ε=0.7 respectively for counter-current and co-current flow configuration. The region highlighted by red color denotes the product as the conversion is completed while the blue region denotes the reactants. The reaction front separates these regions, and it is not a sharp interface as indicated by Figures 6 and

7. The variation in the bed porosity affects the steam transport and in turn results in different reaction front dynamics. In the case of high porosity (ε=0.8), Figure 5, the steam pressure reaches equilibrium everywhere in the bed shortly after the onset of the reaction. Reaction initiates at the steam inlet, and as soon as the steam reaches the other end it triggers the reaction in the entire bed. Hence, soon after the onset of the reaction the direction of the propagating reaction front changes. It starts propagating in the same direction of HTF in the counter flow geometry. In fact, the reaction front propagates in the same direction in both counter-current and co-current flow schemes of steam and HTF except only for a short time after the onset of the reaction.

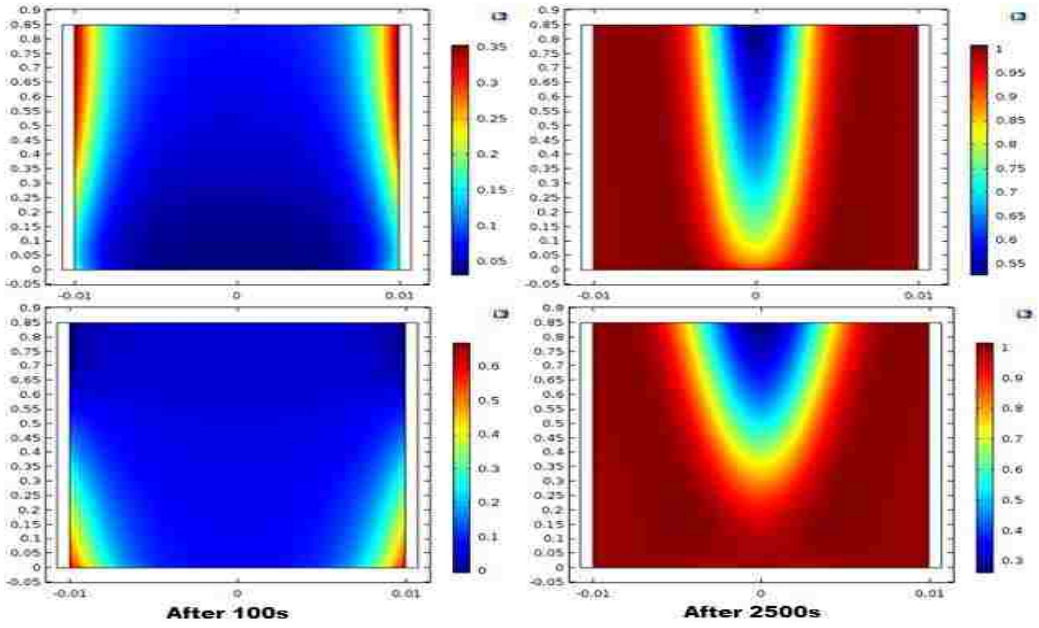

Figure 6. Reaction front for ε=0.8 for counter-current (above) and co-current (below) flow arrangement at early and later stages of the hydration process

As the bed porosity is varied to 0.7 the dynamics of the reaction front and the average of the outlet temperature have been influenced profoundly. Figure 7 shows the reaction front at early and advanced stages of the hydration process in counter-current

and co-current flow geometry for the bed porosity of 0.7. The reaction front propagates in the same direction of the steam flow at all time because of the restriction of the steam transport. Comparison of Figure 5 and Figure 6 for different bed porosities also asserts that the low porosity results in slow reaction due to restricted supply of the reaction gas.

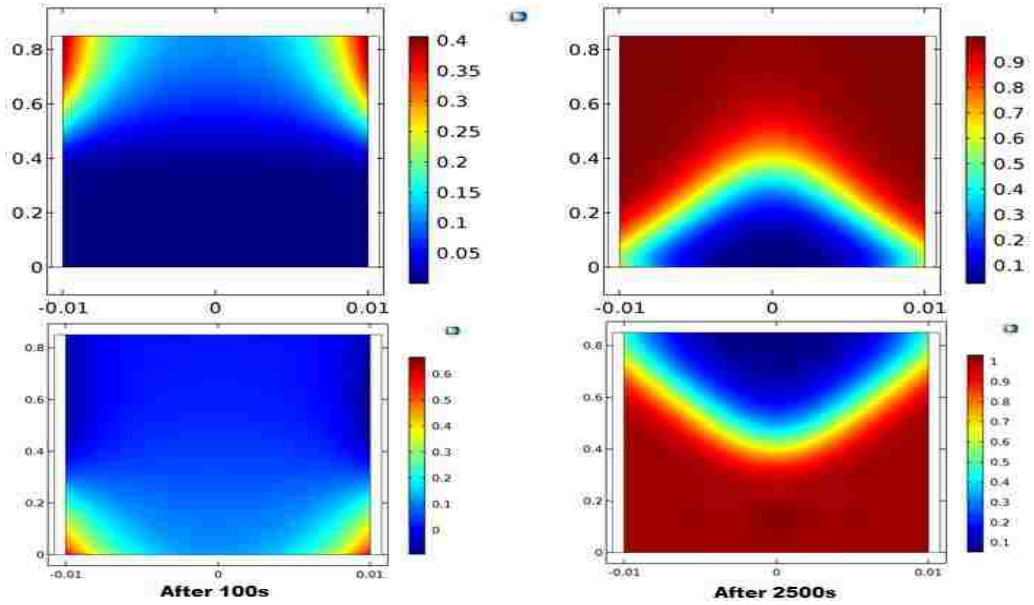

Figure 7. Reaction front for ε=0.7 for counter-current (above) and co-current (below) flow geometry at early and later stages of the hydration process.

The influence of the flow configuration, counter-current, and co-current flow, is also significant when the porosity is varied from ε=0.8 to ε=0.6, as shown in Figure 8. It is noticed that the average outlet temperature is nearly the same for the counter-current and co-current geometry for high porosity (ε=0.8) bed while the average outlet temperature differs noticeably for these geometries when the porosity of the bed is low (ε=0.6).This is because for the co-current flow geometry, the reaction is initiated near the HTF inlet and the heat is released. At the region close to the outlet HTF temperature is

still close to the initial temperature because the steam has not reached there and the exothermic reaction has not been initiated yet.

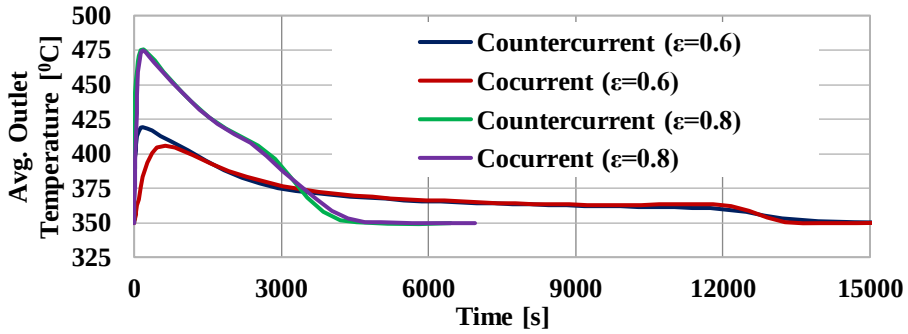

Figure 8. The average temperature of the HTF at the outlet of the bed during the hydration process in co-current and counter-current flow geometry for ε=0.8 and ε=0.6.

Figure 9 depicts a valuable comparison of beds with different porosities in terms of the total conversion time and the maximum outlet temperature in counter-current flow geometry. The difference in the maximum outlet temperature is almost the same when the bed porosity is varied from ε=0.8 to ε=0.7 and from ε=0.7 to ε=0.6 but the increase in the conversion time is greater as the porosity is varied from ε=0.7 to ε=0.6 than that as the porosity is varied from ε=0.8 to ε=0.7.

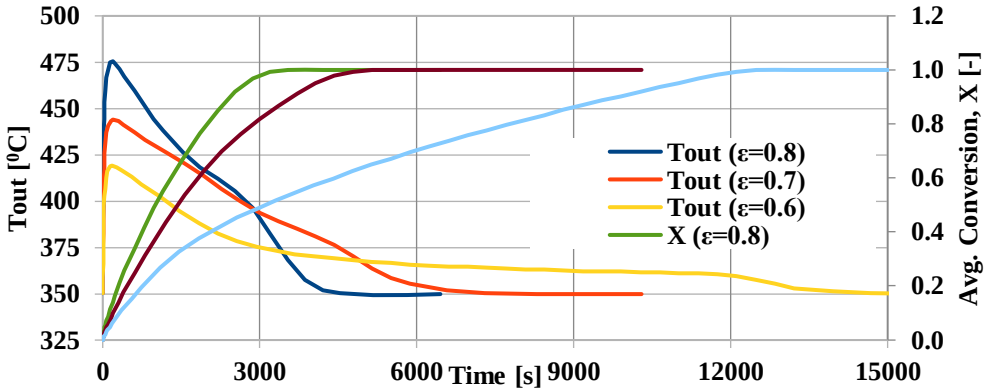

Figure 9. The average temperature of the HTF at the outlet and the conversion as a function of time during the hydration process for the bed porosity of 0.6, 0.7 and 0.8 in counter-current flow geometry.

3.2.3 HTF Inlet Velocity Variations

Heat transfer to and from the bed directly affects the rate of conversion. HTF inlet velocities of 10 m/s, 15 m/s, and 25 m/s were applied, and the result is illustrated in Figure 10. With the three velocities used, flow regime in the HTF region remains laminar. While there is an obvious difference in conversion time, the desired outlet temperature or power input to operate the thermal energy storage module is important factor to determine the HTF inlet velocity. With lower velocity or mass flow rate, not only the outlet temperature reaches higher value but also stays at value for relatively longer time.

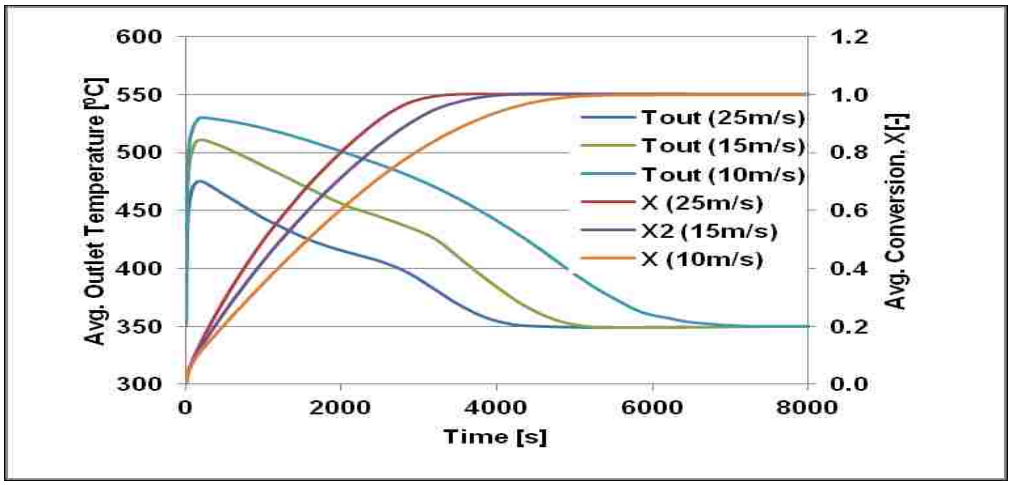

Figure 10. The average temperature of the HTF at the outlet and the conversion as a function of time during the hydration process for the bed porosity of 0.8 in counter-current flow geometry for various mass flow rate of HTF.

3.3 Three-Dimensional Reaction Bed

As it is noticed that the two-dimensional simulations of the rectangular bed yield misleading results in case of lower bed porosities. Also, to get a more realistic representation of the cross flow of the steam and the HTF, it is deemed necessary to carry out the simulations of three-dimensional reactor bed. Figure 2(a) shows an arrangement of reaction beds with HTF channels. The number of beds in the stack is determined by energy input/output requirements. The computational domain in this work includes a single bed with an HTF channel on both sides. Symmetry conditions are applied where symmetry planes run through the middle of HTF channels. The three-dimensional computational domain is shown in Figure 2(b). Material properties and the bed dimensions are listed in Table 1.

Initial and boundary conditions are applied with respect to the coordinates indicated in Table 2. These particular initial and boundary conditions are selected based

on the experimental study [49] of this system for the charging and the discharging process in order to validate the model.

3.3.1 Mesh Study

Equations governing dehydration and hydration processes subject to the boundary and initial conditions are solved using finite element method with COMSOL Multiphysics. Convergence analyses are performed for both the hydration and the dehydration process to ensure the accuracy of the results. An absolute error value of 5x10-5 is set for all the variables in the study. A relative tolerance value of 0.01 is used. Second order tetrahedral elements are used for all variables in the porous bed domain and for heat transfer in the fluid domain. First order prism elements are used for velocity and pressure in the fluid domain.

Time evolution of the temperature, the pressure and the conversion within the bed are calculated at various points inside the bed. Figure 11 shows three half xz- planes at y=0 mm, 400 mm, 840 mm. Points are marked in each plane with odd numbers being at the center and even numbers being adjacent to the bed-HTF interface.

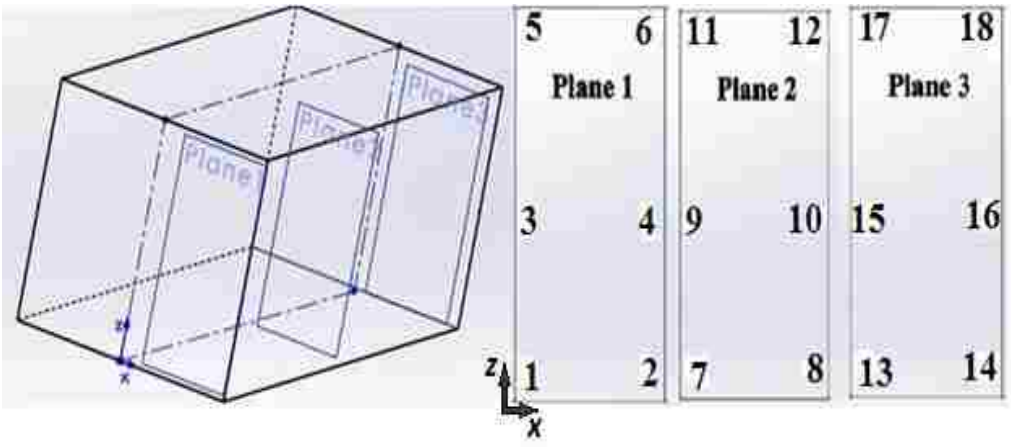

Figure 11. Locations where time evolution of the conversion and the bed temperature is displayed.

These planes are chosen along the length, y-axis, of the bed whereas points on each plane are marked along the width, x-axis, and the height, z-axis, of the bed, as shown in Figure 11. Coordinates of these points are listed in Table 3.

Table 3 Coordinates of points (P) shown in Figure 11.

P	**[mm] (x,y,z)**	**P**	**[mm] (x,y,z)**	**P**	**[mm] (x,y,z)**	**P**	**[mm] (x,y,z)**	**P**	**[mm] (x,y,z)**
1	(0,1,1)	5	(0,1,190)	9	(0,400,100)	13	(0,840,1)	17	(0,840,190)
2	(9,1,1)	6	(9,1,190)	10	(9,400,100)	14	(9,840,1)	18	(9,840,190)
3	(0,1,100)	7	(0,400,1)	11	(0,400,190)	15	(0,840,100)		
4	(9,1,100)	8	(9,400,1)	12	(9,400,190)	16	(9,840,100)		

The mesh density increases towards the bed walls. The mesh is refined in all domains until the results are independent of mesh density selected. Figure 12 shows the time evolution of the temperature and the conversion at a center point (point 9) calculated using different mesh density, n1 = 639852, n2 = 969273, and n3 = 2150969, where n is the total number of elements. It is noted that time evolutions of temperature and conversion are nearly the same for the mesh density of n2 and n3. Hence, the number of mesh n2 = 969273 is used to attain the spatial convergence. Adaptive time steps are employed for the temporal convergence.

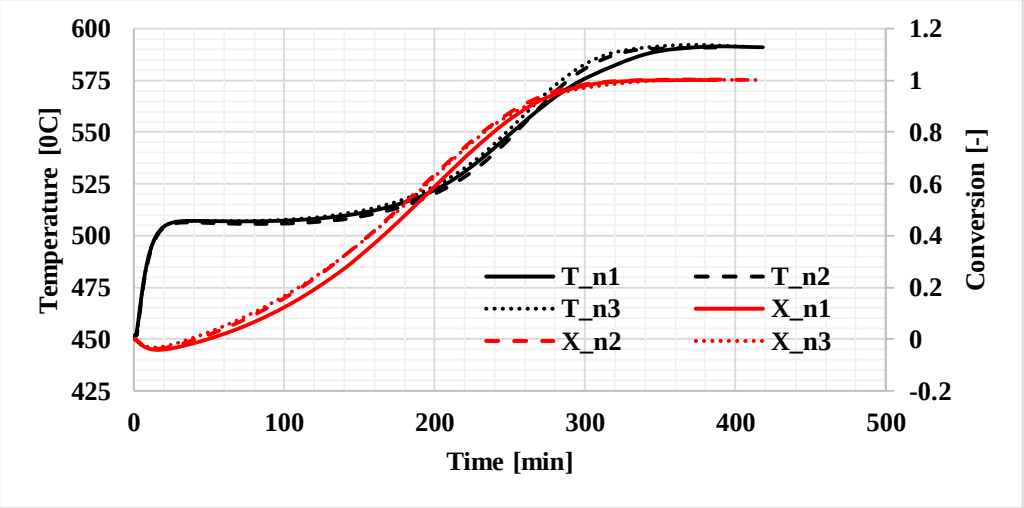

Figure 12. Time evolution the temperature and the conversion for the dehydration process at the point (0mm,400mm,100mm) for the mesh density of n1 = 639852, n2 = 969273, and n3 = 2150969. Here n denotes the number of elements.

3.3.2 Results and Discussion

Charging and discharging processes were simulated with constant HTF inlet velocity of 25m/s. With specified dimensions of the HTF channel and temperature

of the air, flow remains laminar at all times during the charging and the discharging process.

Figure 13 shows the evolution of temperature at various points indicated in Figure 11 for the dehydration process at a constant porosity of 0.5. Initially, the bed and HTF are in a thermal equilibrium at $T_{ini/D}$=450^{0}C and the bed pressure $P_{ini/D}$ is equal to the reaction equilibrium pressure corresponding to the initial temperature of 450^{0}C. Under these conditions of pressure and temperature the forward reaction (dehydration) will commence as soon as the bed temperature exceeds the equilibrium temperature. A constant temperature $T_{inlet/D}$=590^{0}C is applied at the HTF inlet to keep the bed temperature well above the equilibrium temperature $T_{eq/D}$.

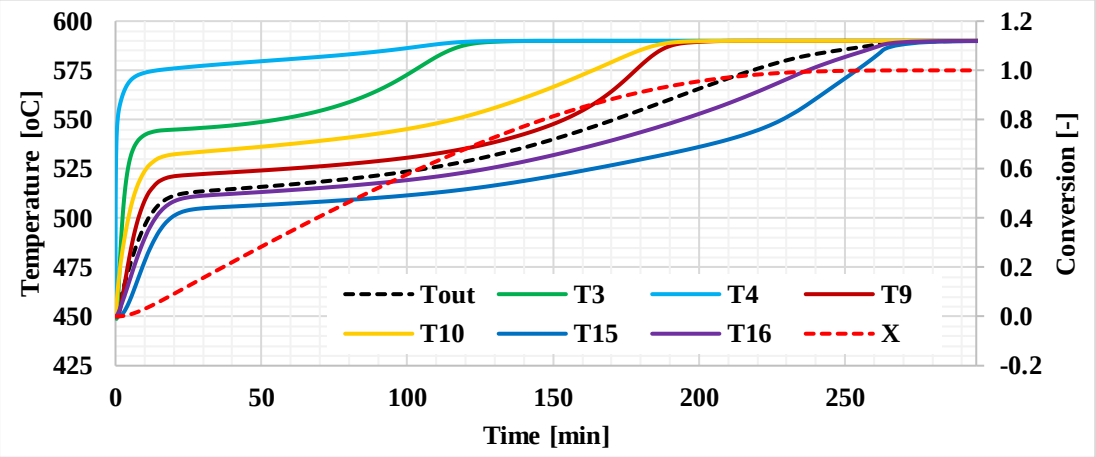

Figure 13. Time evolution of the bed temperature at center points of three planes, the HTF average outlet temperature and the average conversion during the charging process (the dehydration process

Dehydration proceeds with heat transfer from the HTF to the bed. Bed temperatures at various points, the average value of the outlet temperature of HTF, and the average conversion are plotted as a function of time in Figure 13. Temperatures of the bed near the interface (T4, T10, and T16) rise rapidly at the beginning followed by a

gradual increase in time to the HTF temperature. Temperatures at the center of the bed (T3, T9, and T15) rise rapidly at the early stage, remain nearly constant at the intermediate stage, and upsurge again to the HTF temperature. This behavior can be explained using the fact that the endothermic reaction starts after the initial temperature rise above the equilibrium temperature which results in activation of a heat sink with the generation of steam. The steam generated also increases the bed pressure resulting a corresponding increase in the reaction equilibrium temperature according to equation (25). Consequently, the equilibrium temperature in the middle of the bed rises slightly above the bed temperature for a very short time at an early stage triggering the reverse reaction in that region. This is indicated by the conversion profiles X3, X9, and X15 depicted in Figure 14.

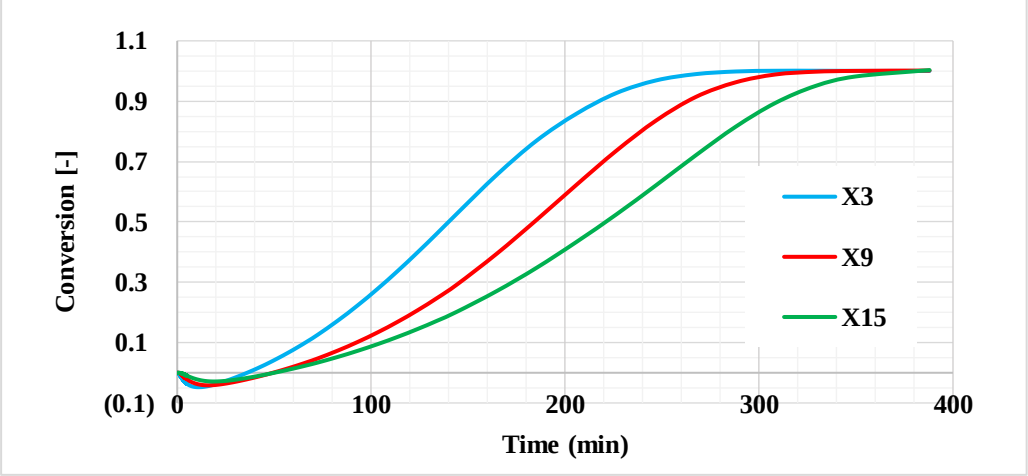

Figure 14. Conversion at points 3, 9 and 15 as a function of time during the dehydration process

Such behavior is observed only in a three-dimensional geometry. The reverse reaction vanishes as the bed pressure starts decreasing as the steam starts leaving the bed.

As a result, the equilibrium temperature again becomes lower than the bed temperature in the middle.

Hydration (the discharging process) is depicted in Figure 15. Time evolution of bed temperatures at the center of three planes (Points 3, 4, 9, 10, 15, and 16), the average outlet temperature of HTF and the average conversion are shown. This reverse exothermic reaction is simulated by assuming that the bed and HTF initially are at the same temperature $T_{ini/H}$ =350^{0}C and that the bed pressure $P_{ini/H}$ is equal to the equilibrium pressure corresponding to 350^{0}C determined by equation (25). The reaction gas (steam) is then introduced from the top face at a pressure of 198 kPa. This pressure is held constant for the entire process. Reaction equilibrium temperature for this pressure is around 550^{0}C. Therefore, the maximum temperature that can be reached within the bed is 550^{0}C. Inlet air temperature is kept constant at 350^{0}C which is well below the reaction equilibrium temperature corresponding to the steam inlet pressure. The reaction starts with generation of heat which is transferred to the HTF through the bed walls. A sudden increase in the bed temperatures is due to the spontaneous release of heat as the steam moves through the bed and is reacted with the CaO powder, as indicated in Figure 15.

After the initial sudden rise, bed temperatures near the interface (points 4,10,16) gradually decrease to HTF temperature. On the other hand, after the initial impulsive increase bed temperatures near the center (points 3,9,15) still increases gradually towards the reaction equilibrium temperature (550^{0}C) and then decrease rapidly to the HTF temperature.

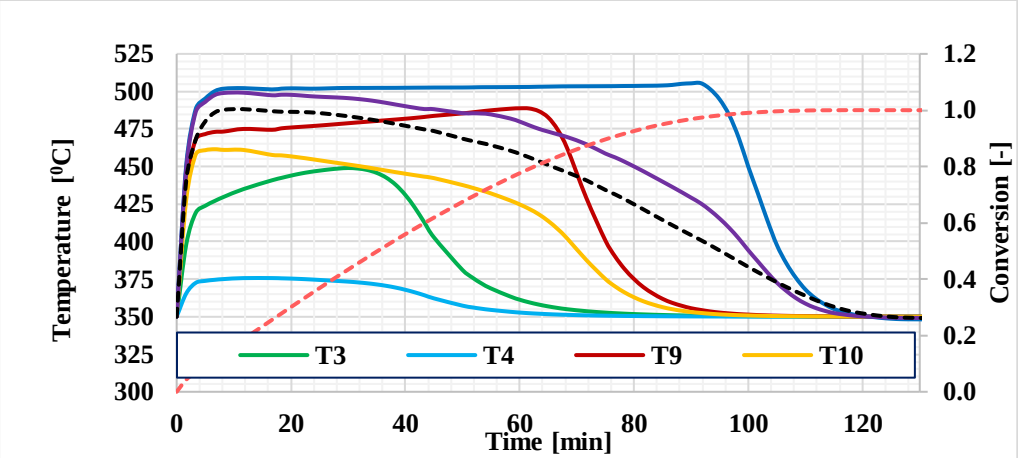

Figure 15. Bed temperatures during the discharging process (hydration process), HTF average outlet temperature and the average conversion. Bed temperatures are recorded at locations that are shown in Figure 11.

This is due to the delayed heat transfer from the center. Steam moving through the bed increases the bed pressure which results in an increase in the reaction equilibrium temperature reaching. The bed temperature must be kept below the equilibrium temperature for the conversion to proceed. Figure 16 shows the bed temperature, the reaction equilibrium temperature and the conversion at point 9 as a function of time. It is clearly seen that the conversion at this particular point in the middle of the bed accelerates after about 50 minutes. At this point the bed temperature T9 starts to drop lower than the reaction equilibrium temperature Teq9 due to heat removal from the bed.

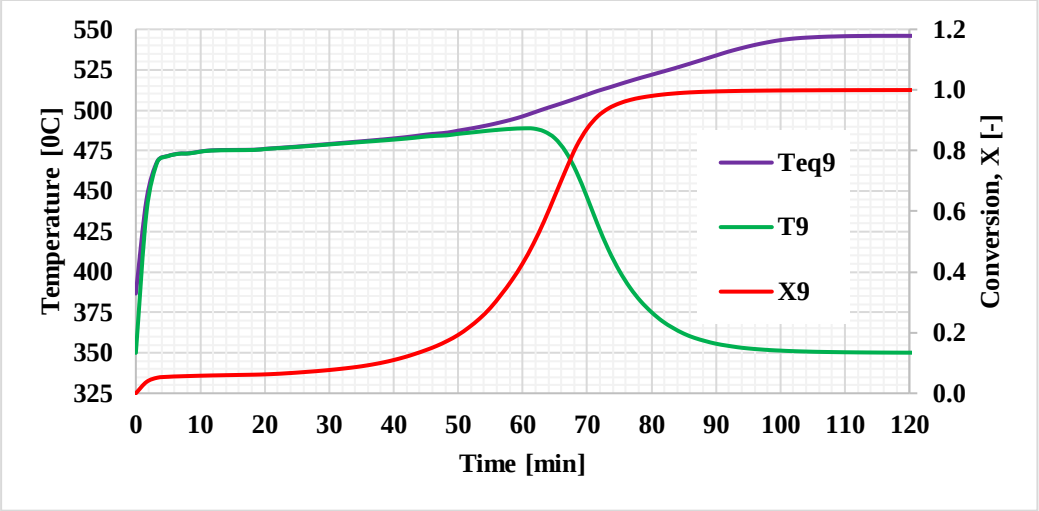

Figure 16. The reaction equilibrium temperature, the bed temperature and the conversion at point 9 as a function of time.

3.3.3 Model Validation

Results presented here are compared against experimental results for the indirectly heated three-dimensional rectangular packed bed [49] operating at similar conditions. They are also compared against those predicted for the two-dimensional packed bed of the same system [50]. Due to the unavailability of the exact experimental data and precise locations of thermocouples for experimental results [49] a quantitative comparison of results is neither possible nor appropriate. However, a qualitative comparison of the temperature within the bed and of HTF at the outlet is made. In the case of hydration, the time evolution of bed temperatures and the total conversion are shown in Figure 8 of Ref [49]. These temperatures are measured at points along the length of the bed. Exact coordinates of these points are not provided in Ref [49]. It can be seen that the heat transfer from the bed is the primary factor that determines characteristics of the temperature and the conversion. Temperatures (T_1, T_5) near the inlet of HTF shown in Figure 8 of [49] have sharper decline after reaching the maximum value

due to enhanced heat transfer. This behavior is evident in results in the Figure 15 of this study where bed temperatures closer to the wall (points 3,9,15) have higher gradients than those at the center (points 4,10,16). The average value of the outlet temperature is shown as black dotted line in Figure 15 of this study. Maximum calculated value is 488^0C as compared to the measured value 475^0C reported in [49]. The measured value might have been recorded using a single thermocouple so it may not represent the average outlet temperature.

Dehydration has different characteristics compare to hydration as can be seen in Figure 13 of the present study and Figure 7 of the experimental study [49]. Given the fact that the conversion was reported to be incomplete in [49], theoretically the bed and the HTF come in equilibrium at temperature equal to the inlet temperature of the HTF, as shown in Figure 13 in this study. However, the bed and the HTF reach to a different equilibrium temperature in the experiment as depicted in Figure 7 of [49]. The difference in the maximum temperature reached at different locations in the bed and the total conversion time between experimental and simulation results can be attributed to various factors. One important issue is channeling and sintering effects in experiments resulting from the steam flow through the bed as reported in [8]. The reaction rate in the present study is calculated as function of temperature using Arrhenius equation (19). Values of the activation energy (E) and the pre-exponential factor (A) used to determine the reaction rate have been reported over a range of values for both the hydration and the dehydration processes. The difference in the reported values of E and A is higher in the case of dehydration process compared to hydration process. Hence, the values used here may not be the true approximations of the reaction rate for the material sample used in

the experiments of [49]. Other important factors contributing to the deviations are approximations made in using the values of porosity, thermal conductivity, and boundary conditions.

In order to validate their model against their own experiments P. Schmidt and M. Linder [50] performed simulations in a two-dimensional reactor and heat exchanger set up. They presented hydration results for a high porosity of bed (ε~0.8). In order to obtain a reasonable level of agreement they introduced a heat loss term adapted to their own experiments. In addition to the heat loss and several other factors adding up to the deviations as discussed above, most importantly, a two-dimensional reaction bed itself may not be a good representation of the process if more realistic porosity value of the powdered bed (ε~0.5) is used in the simulations. Next section embraces more details on three-dimensional effects.

3.3.4 Low Porosity Bed

In addition to the modeling of prototyped dehydration and hydration process this work is aimed at examining three-dimensional effects in cases of poorly permeable beds. Poorly permeable beds are desirable in a way that a low porosity will yield a high volumetric energy density resulting in more compact beds for the same power output. Particle porosity of the solid powder generally being a constant parameter for the given particle size, the bed porosity depends on the infilling process. The porosity of the bed may vary from 0.5 to 0.8 depending on how densely it is packed with the powder.

Figure 17 shows temperature contours over three parallel xy-planes during the hydration reaction for ε = 0.5. Hydration starts as soon as the steam is introduced from

the top and the temperature at the top plane reaches the reaction equilibrium temperature shortly after that. The reaction equilibrium temperature is greater closer to the HTF outlet, as shown in contours at 100 seconds. This is due to the fact that the rate of heat transfer from the bed to HTF is greater near the HTF inlet as a result of larger temperature gradients. Temperatures at lower planes start to increase later as the steam penetrates to these planes and the exothermic reaction commences. As can be seen at 3500s the temperature in the middle and lower planes start to rise while most of the top planes have already been cooled.

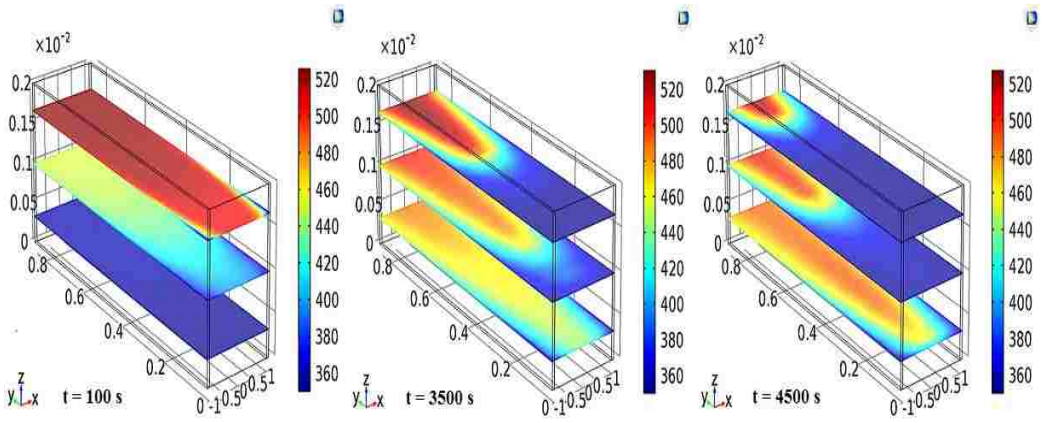

Figure 17. Temperature contours over three parallel xy-planes at t = 100s, 3500s, and 4500s Images are acquired in the bed with ε = 0.5 during the hydration process.

Figure 18 shows conversion profiles of vertical planes located along the length of the bed at t = 2000s during the exothermic hydration reaction for ε = 0.5. The reaction front propagates both in the x- and y-direction. This indicates that three-dimensional effects are profound in the low porosity bed.

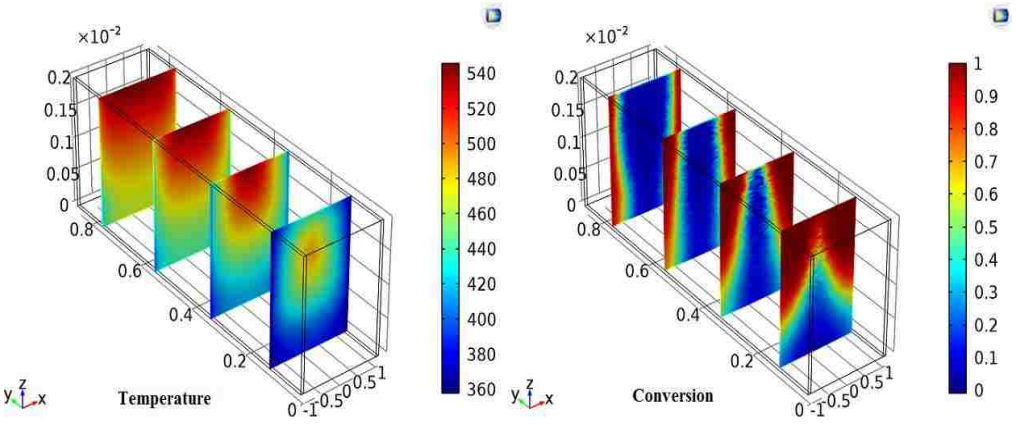

Figure 18. Temperature and conversion profiles over xz-planes along the length of the bed at t = 2000s.

In order to verify three-dimensional effects observed in the low porosity bed simulations are conducted for the high porosity bed ($\varepsilon = 0.8$) for the hydration process. Figure 19 shows temperature contours over three xy-planes at three instants during the exothermic reaction. Steam moves with little resistance in the high porosity bed so it is available almost instantly everywhere. Consequently, the exothermic hydration reaction commences everywhere shortly after the beginning of the steam supply from the top resulting heat release and the bed temperature rise almost equally everywhere. Similar temperature contours, therefore, can be seen at each horizontal plane at all times during the reaction. By comparing the temperature contour at 100s in Figure 19 to the temperature contour at 100s in Figure 17, it can be seen how the restricted supply of steam can delay the exothermic reaction in the case of low porosity. Also, it can be seen that the maximum temperature reached in highly porous bed (Figure 19) is around 540^0C whereas the maximum bed temperature reached in low porosity bed (Figure 17) is around 520^0C. This is because the steam pressure inside the low porosity bed does not increase as rapidly as it does in high porosity bed. As a result, the reaction equilibrium

temperature in the low porosity bed does not reach to the maximum value in most of the parts corresponding to the inlet pressure. So, the reaction in those areas occurs at lower pressure than the inlet pressure resulting in lower heat of reaction.

Based on these results, transports in the high porosity reaction bed can be modeled using a two-dimensional geometry. However, two-dimensional approximation of the low porosity bed will not be able to capture temporal and spatial characteristics of the thermo-chemical energy storage/retrieval.

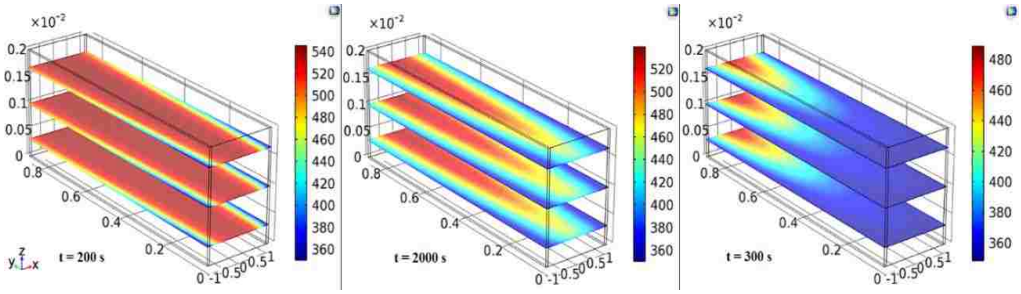

Figure 19. Temperature contours over three parallel xy-planes at t = 100s, 2000s and 3000s during the hydration reaction with ε = 0.8

3.3.5 Effect of Particle Size

The model is validated against available experimental results in [49]. The developed model give reasonably good predictions of the charging and discharging processes for the indirectly heated $Ca(OH)_2/CaO$ fixed beds. However, it is important to discuss the limitations of applying the model and challenges in using this reaction system $Ca(OH)_2/CaO$. It is established that heat and mass transports in these beds are strongly three dimensional in case of poorly permeable beds. The permeability of the bed is related to bed porosity and particle size through equation 6. Effect of the bed porosity is presented in section 3.3. Constant values of the bed porosities are used in this study

because of the small particle size. Porosity variation in transverse or radial (in case of circular bed) direction should be included in the model if particles with greater size (order of mm or higher) are used. Effect of varying particle size on the conversion time is shown in Figure 20. It can be seen that the total conversion time is decreased when the particle size is increased from 5µm to 10µm. But the time remains same for the diameters 10µm, 20µm and 50µm. Although, an increase in permeability increases mass transfer within porous media, it is also accompanied by decreased heat transfer within the bed. Hence, there is a range of permeability for a constant value of porosity where change in particle size can influence the overall conversion. Also, for larger particle sizes the reaction mechanism displayed in equation (20) should be modified accordingly.

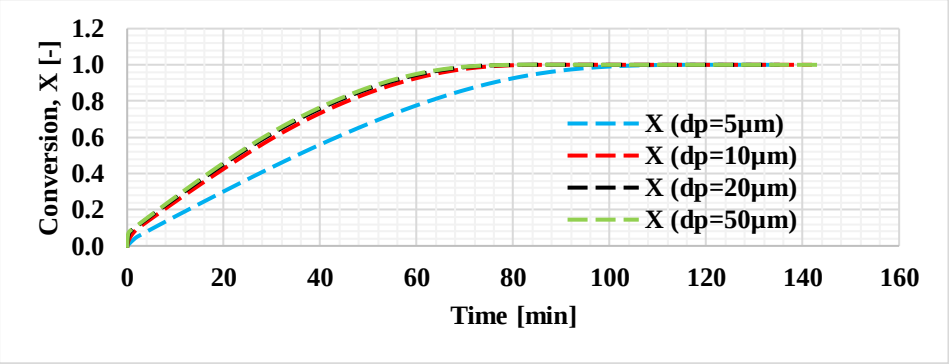

Figure 20. Average conversion profiles for various particle sizes.

3.4 Summary

Two-dimensional and three-dimensional geometries of the rectangular fixed reactor bed are simulated. The reactor bed is indirectly heated/cooled from the side walls by HTF. Both charging and discharging processes are simulated using COMSOL Multiphysics. The results presented show good agreement with the experimental results of the similar system [49]. A rather good agreement between the predicted results and

those obtained from experiments will, however, require a careful selection of geometrical and operational parameters. Values of key reaction parameters depend on the material sample and experimental condition under which they are determined. Hence, values of reaction enthalpy and Arrhenius parameters are found over a range in the literature. The process is strongly three-dimensional for a lower porosity bed ($\varepsilon < 0.7$). The comparison of our results with previous experimental results [49] yields interesting insight into the conflicting parameters dictating energy storage and retrieval process. The porosity of the bed should be kept low for high energy density, but this will restrict flow of reaction gas moving through the bed resulting in slow reaction or a reverse reaction in certain instances. Conversely, a highly porous bed gives better reaction rates but with lower energy input/output. Two parameters, thermal conductivity and porosity, limit upscaling of the single bed. The low thermal conductivity prohibits an increase in width to keep the length of the heat transfer path short. The porosity value dictates the height of the bed for the steam flow. The storage capacity of the reactor can be increased by arranging the multiple rectangular beds and HTF channels in parallel [49] as shown in Figure 2. However, increase in size (height and width) of a single bed will affect the storage and discharge processes to a great extent. Increasing height of the bed, particularly the low porosity bed, will restrict the steam flow within the bed whereas increasing width will affect the heat transfer to/from the bed due to poor conductivity of the materials. Increasing the width of a single bed with lower porosity will require heat transfer enhancement techniques. These techniques applied to the circular reaction beds with different flow configurations of the HTF are discussed in the next chapter.

CHAPTER 4 CIRCULAR BED WITH HEAT TRANSFER ENHANCEMENTS

Circular geometry offers certain advantages over the rectangular geometry regarding heat transfer. In this chapter, various reactor configurations using circular reaction beds are considered, and the mathematical model is used to simulate hydration and dehydration reactions in each of the configuration. In order to enhance the heat transfer within the porous bed, heat transfer enhancement techniques are introduced, and their effect on conversion is studied and compared.

4.1 Reactor Configurations

Fixed circular reaction bed packed with fine particles of $Ca(OH)_2/CaO$ is considered with two HTF channel configurations. Numerical simulations of the dehydration and the hydration reaction are carried out. Figure 21 shows the proposed reaction bed and the HTF channel configurations. Configuration 'a' uses an outer annular shell for the flow of HTF whereas the configuration 'b' uses an internal pipe as an HTF channel. Counter-flow scheme between the HTF (air) and the reaction gas (steam) is used where steam enters the reaction bed from the top, and HTF enters from the bottom. The height of the reactor in each configuration is kept the same at $h_r = 200mm$. For comparison of two reactor configurations, the volume of the reaction bed is held constant. Size of the HTF channel in both reactors is determined for the fixed value of Reynolds number, Re, and the inlet air velocity. $\mathrm{Re} = \frac{(\rho U)_{air} D_h}{\mu_{\mathrm{air}}}$, where ρ is the density of air, U is the average air velocity, μ is the dynamic viscosity of the air, and D_h is the hydraulic diameter of the HTF channel. Reynolds number of 1500 and HTF inlet velocity of 25m/s

are used in each case to determine the size of the HTF channel. Physical parameters employed are listed in Table 1.

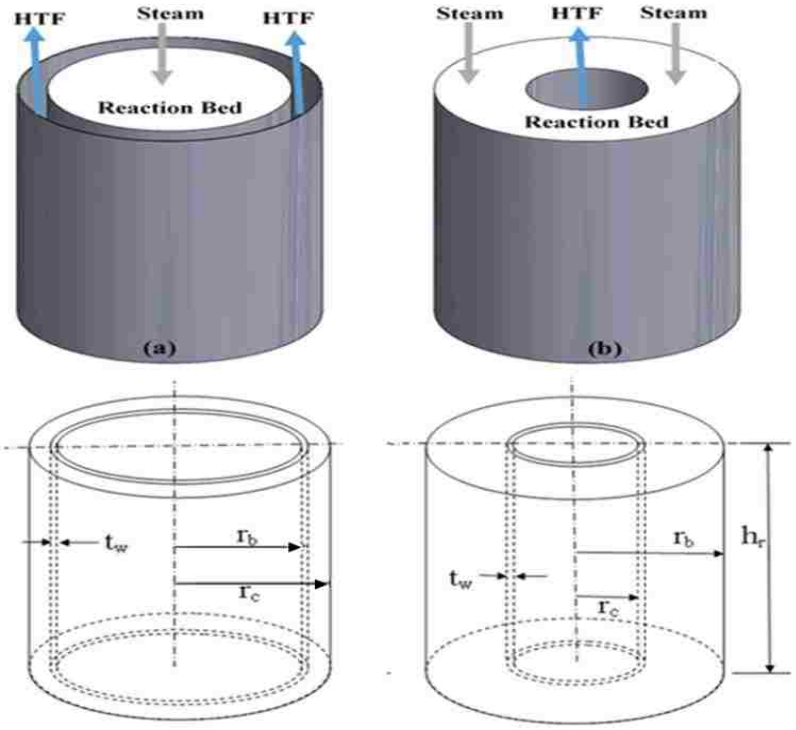

Figure 21. Reaction bed configurations with (a) an outer annular and (b) an internal pipe as HTF channels. Dimensions of each reactor are displayed.

4.2 Heat transfer Enhancements (HTE)

The wall between the HTF channel and the bed is augmented with fins of the same thickness to enhance the heat transfer within the reaction bed. The fins extend into the bed to a depth of $0.75 \times r_b$ in the reactor 'a' and $r_c + 0.75 \times (r_b - r_c - t_w)$ in the reactor 'b'. Dimensions of each reactor are depicted in Figure 20 and the reactors with finned wall are shown in Figure 22.

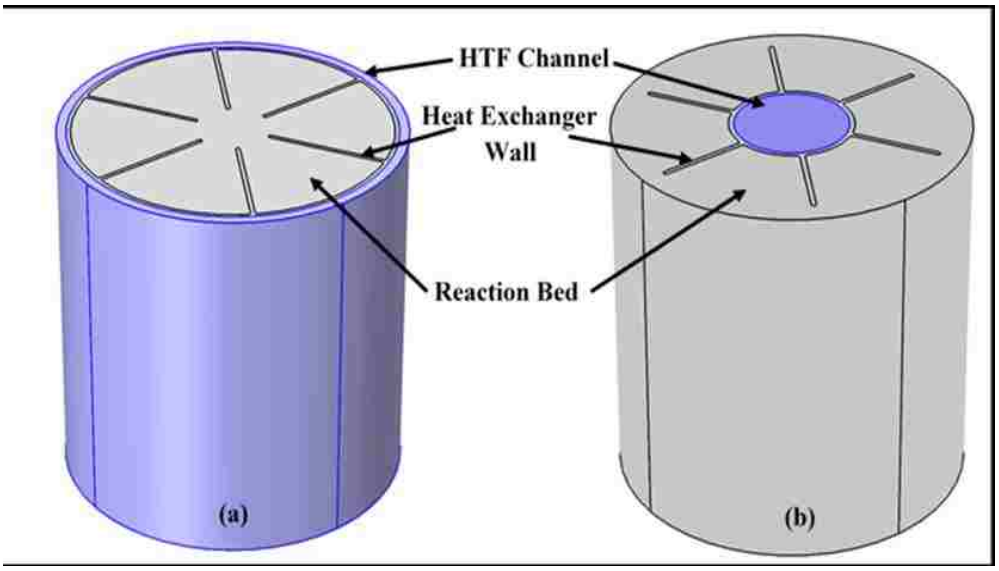

Figure 22. Reactors shown in Figure 21 with fins attached to the wall between the bed and the HTF channel.

Presence of fins breaks the symmetry and leads to a non-axisymmetric velocity and temperature field. The low bed porosity of 0.5 used in this study causes axial variations in the temperature and velocity field. As a result, both flow and temperature field are expected to display strong three-dimensional structures in the reactor. It is established in the previous chapter that the bed porosity $\varepsilon \leq 0.6$ leads to three-dimensional transports within the bed due to the slower flow of the reaction gas (steam).

The same governing equations are used as in the previous chapter. An additional energy conservation equation for the wall between the HTF channel and the reaction bed is used here instead of using conjugate heat transfer because the heat transfer enhancements are carried out through fins attached to the wall. The wall energy equation is given as

Initial and boundary conditions for the governing equations are given in Table 4.

Table 4 Initial and Boundary Conditions circular beds

Eqns	Boundary/initial condition	Description
7,14,15	At $t = 0$ $T_{Bed} = T_{HTF} = T_{Wall} = T_{ini_H} = 350℃$	Initial reactor Temperature (hydration)
7,14,15	At $t = 0$ $T_{Bed} = T_{HTF} = T_{Wall} = T_{ini_D} = 450℃$	Initial reactor Temperature (dehydration)
7	At $h = 0, h_r$ and $r = r_c$ $-n.\mathbf{q} = 0$ $\{\mathbf{q} = -K\nabla T\}$	Insulated walls of the reactor 'a'
7	At $h = 0, h_r$ and $r = r_b$ $-n.\mathbf{q} = 0$ $\{\mathbf{q} = -K\nabla T\}$	Insulated walls of the reactor 'b'
14	At $r = (r_c + t_w), r_b$ $u_{HTF} = 0$	No slip (reactor 'a')
	At $r = (r_c + t_w), r_b$ $u_{HTF} = 0$	No slip (reactor 'b')
14	At $\begin{cases}(r_c + t_w) < r < r_b \\ h = 0\end{cases}$ $u_{HTF} = 25\ m/s$	Inlet velocity of HTF (reactor 'a')
	At $\begin{cases}0 < r < r_c \\ h = 0\end{cases}$ $u_{HTF} = 25\ m/s$	HTF inlet velocity (reactor 'b')
14	At $\begin{cases}(r_c + t_w) < r < r_b \\ h = 0 \\ t > 0\end{cases}$ $T_{HTF_H} = 350℃, T_{HTF_D} = 550℃$	HTF inlet Temperature (reactor 'a')
	At $\begin{cases}0 < r < r_c \\ h = 0 \\ t > 0\end{cases}$ $T_{HTF/H} = 350℃,\ T_{HTF/D} = 550℃$	HTF inlet Temperature (reactor 'b')
3,5	At $\begin{cases}t = 0 \\ 0 < r < r_b\end{cases}$ $P = 3000$ pa At $\begin{cases}h = h_r \\ 0 < r < r_b\end{cases}$ $P = 200000$ pa	Initial pressure and steam pressure at the top inlet; hydration
3,5	At $\begin{cases}t = 0 \\ 0 < r < r_b\end{cases}$ $P = 13300$ pa At $\begin{cases}h = h_r \\ 0 < r < r_b\end{cases}$ $P = 13300$ pa	Initial pressure and steam pressure at the top outlet; dehydration

Table 4 (Continued……)

3,5	$\text{At } \begin{cases} h = 0 \\ 0 < r < r_b \end{cases} \quad -n.\rho u_{st} = 0$ $\text{At } \begin{cases} r = r_b \\ 0 < h < h_r \end{cases} \quad -n.\rho u_{st} = 0$	No mass flux; hydration and dehydration (reactor 'a')
3,5	$\text{At } \begin{cases} h = 0 \\ (r_c + t_w) < r < r_b \end{cases} \quad -n.\rho u_{st} = 0$ $\text{At } \begin{cases} r = r_b \\ 0 < h < h_r \end{cases} \quad -n.\rho u_{st} = 0$	No mass flux; hydration and dehydration (reactor 'b')

4.3 Numerical Solution

Coupled set of equations (3) through (16), (25) and (26) is solved numerically using finite elements with COMSOL Multiphysics. Quadratic tetrahedral elements are used for conversion, steam transport within the bed and heat transfer within the wall. First order tetrahedral elements are used for heat transfer within the bed whereas first-order tetrahedral and prism elements are used within HTF domain. Mesh is refined in all domains until temperature and conversion profiles are independent of mesh density. Temporal convergence is achieved using adaptive time steps. An absolute tolerance value of $5x10^{-5}$ and a relative tolerance value of 0.01 are set for all variables. Results of the mathematical model were validated in previous studies against the experimental results [49] for rectangular and circular reaction beds. The validity of the model and the numerical settings were established in these studies and is, therefore, not repeated in this work.

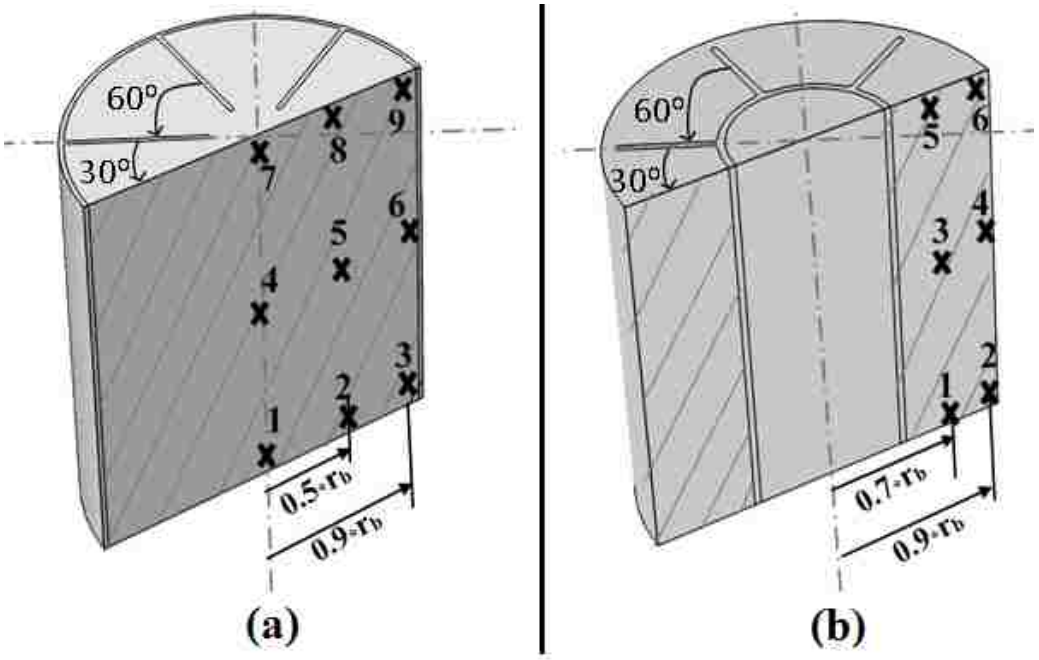

Figure 23. Locations where time evolution of temperature is displayed.

Instantaneous temperature is recorded on a vertical plane through the bed axis in the middle of the two fins in both reactors in cases of the finned wall. The cut planes and the radial location of points are shown in Figure 23. The points are marked along the height of the bed at $0.01 * h_r$, $0.5 * h_r$ and $0.95 * h_r$. The same probe points are used for the reactors without fins for proper comparison.

4.4 Results and Discussion

4.4.1 Dehydration (Charging)

Time evolution of temperature at various locations and the average conversion during the dehydration process in the reactor 'a' with $r_b = 10\,mm$ are shown in Figure 24. Size of the HTF channel in all the configurations is determined by keeping the inlet velocity at 25m/s and Reynolds number constant at 1500. The temperature at points in the

middle of the bed (points 2,5,8) and along the bed axis (points 1,4,7) and the average conversion of the reactants into the products are shown as a function of time. At the start of the dehydration the whole reactor is set in the thermal equilibrium at 450^0C and, the bed pressure is set equal to the equilibrium pressure corresponding to this temperature according to equation (25). The inlet temperature of the HTF is set at 550^0C for t > 0 to allow the heat transfer from the HTF to the bed. Dehydration reaction initiates as soon as the bed temperature rises above the equilibrium temperature within the bed. Reaction equilibrium temperature within the bed also changes with the bed pressure due to steam generation. In order to avoid the re-hydration reaction, the bed temperature should be higher than the equilibrium temperature of dehydration. At the end of the dehydration process, the whole reactor comes in thermal equilibrium at the HTF inlet temperature.

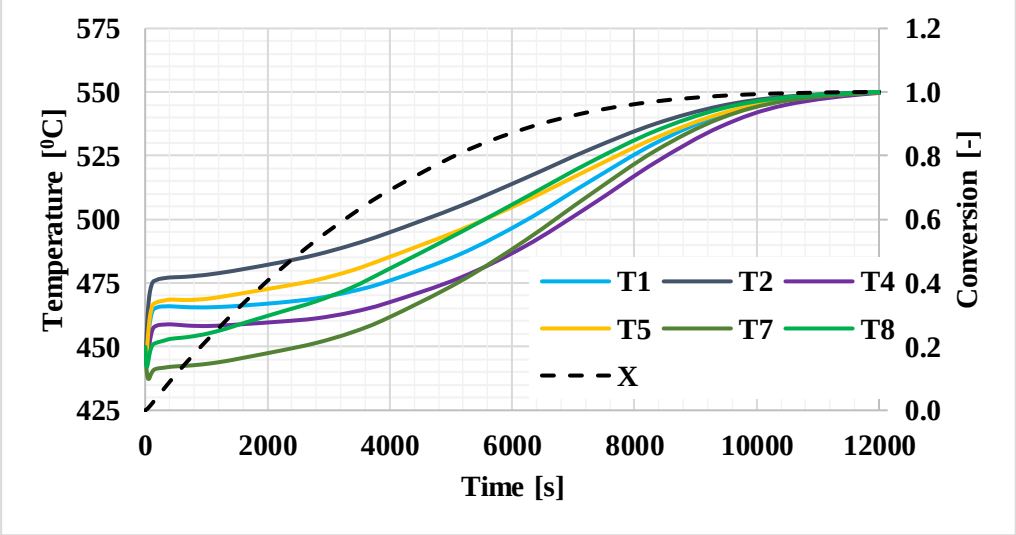

Figure 24. Temperature at the points within the bed (without fins) shown in Figure 23(a) and average conversion during the dehydration process ($r_b = 10\ mm$)

The temperature at the locations (4,7,8) away from the HTF inlet drops below the initial temperature due to the slow rate of heat transfer to these regions within the bed. At

the early stage of the dehydration, the reaction starts in the regions close to HTF inlet (points 1,2,5) and the heat sink is activated which causes the temperature to drop slightly in the upper and the middle parts since the rate of heat transfer from HTF is not fast enough. Such temperature drop does not occur in the reactor with the finned wall, as shown in Figure 25.

Time evolution of temperature at three points (1,4,7) located along the axis is plotted for the reactor 'a' with and without fins for comparison in Figure 25. The dotted and solid lines denote evolution of the temperature and conversion in the reactor with and without fins, respectively. The average conversion time in a reactor with and without fins is 8000s and 11000s, respectively. The conversion in the finned reactor is about 27% faster compared to that in the reactor without fins.

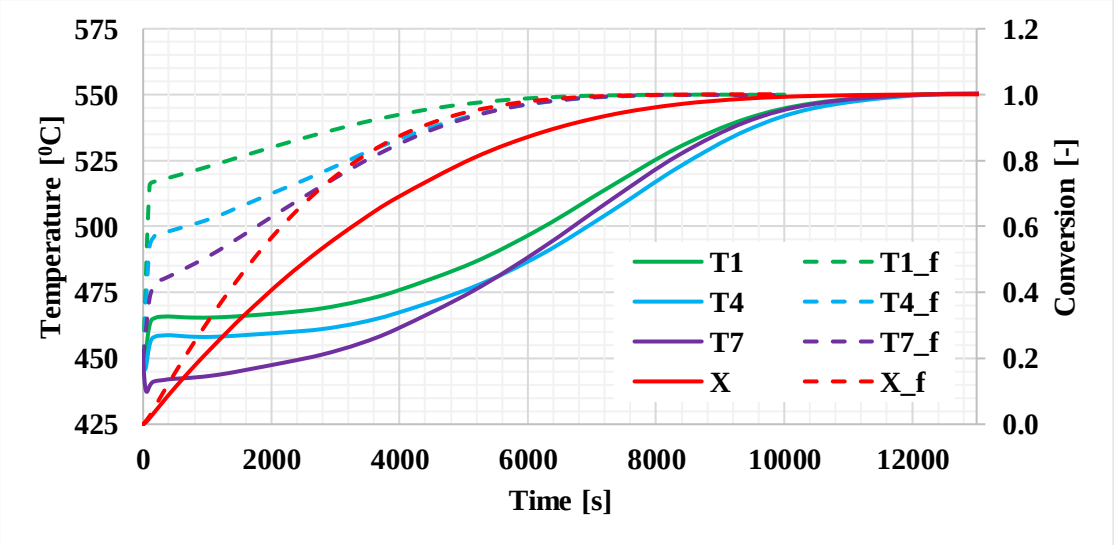

Figure 25. Average conversion and temperature along the bed axis of the reactor 'a' with fins (dotted lines) and without fins (solid lines) during the dehydration process($r_b = 10\,mm$).

4.4.2 Hydration (Discharging)

Results of the hydration reaction for the reactor 'a' without fins are presented in Figure 26 which shows the bed temperatures at points in the middle of the bed (2,5,8) and at the bed axis (1,4,7) along with the average conversion during the energy discharge process. The hydration process is initiated by setting the whole reactor in the thermal equilibrium at 350^0C, and the bed pressure equals to the equilibrium pressure determined from the initial equilibrium temperature using equation (25). HTF inlet temperature is also set at the same temperature (350^0C) for t > 0 to allow the heat transfer from the bed to the HTF after the onset of the exothermic reaction within the bed. Steam inlet pressure is set at 2 bar for which the equilibrium temperature is 550^0C. The reaction initiates with steam transport within the bed. Heat is generated from the exothermic reaction with a sudden rise in the bed temperature. Also, the reaction equilibrium temperature rises with an increase in the steam pressure according to equation (25). The bed temperature needs to be kept below the equilibrium temperature of dehydration to avoid the reversed reaction.

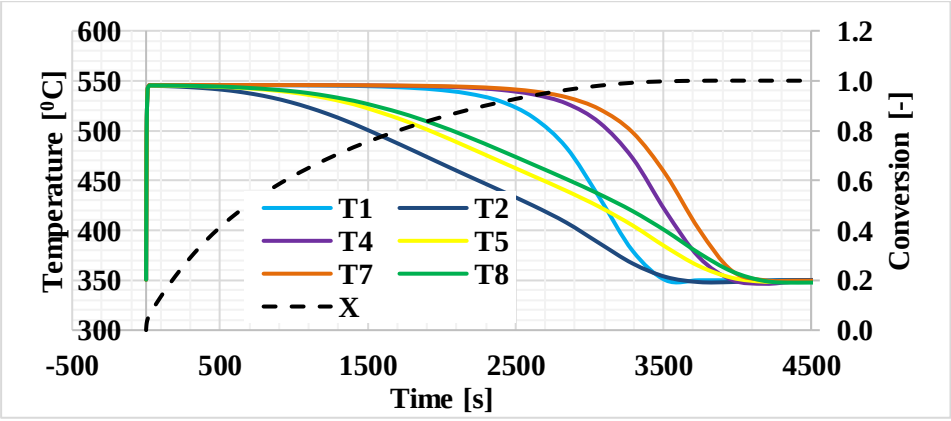

Figure 26. Temperature at the points within the bed (without fins) shown in Figure 23(a) and average conversion during the hydration process ($r_b = 10\ mm$).

Figure 27 depicts the time evolution of temperature at various points and the conversion during the hydration process in the reactor ‘a' with and without fins. The temperature at three points (1,4,7) along the bed axis and the average conversion are compared. Dotted lines represent the profiles with HTE whereas the solid lines represent the profiles without HTE. Average conversion time in the finned wall reactor is 1400s whereas it is 4000s in the reactor without fins. The conversion time is reduced by almost 65% in the reactor with fins compared to that in the reactor without fins.

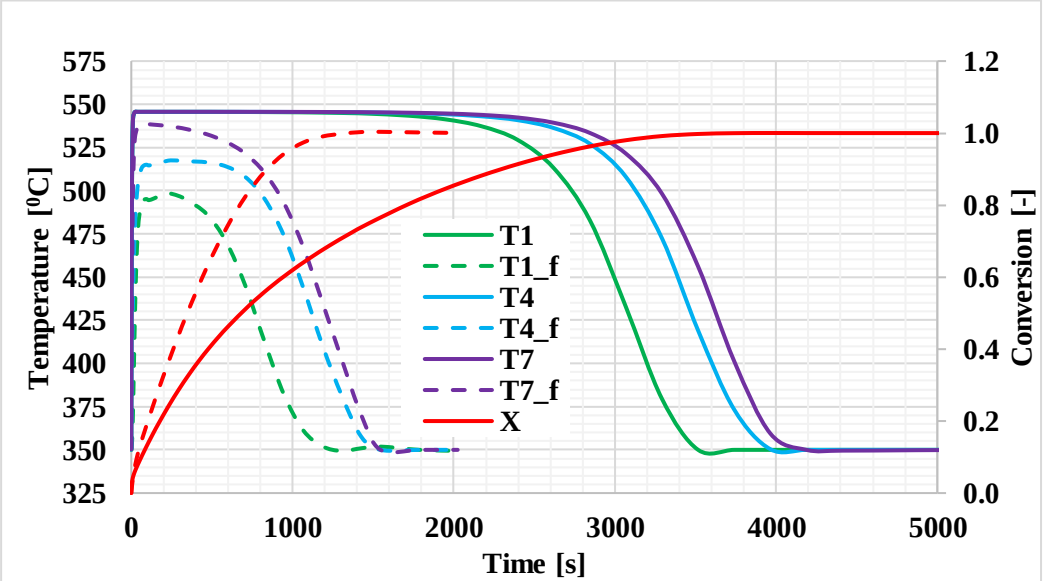

Figure 27. Average conversion and temperature at points 2, 4 and 6 in the reaction bed of the reactor 'b' with fins (dotted lines) and without fins (solid lines) during the hydration process.

The heat transfer enhancement with fins is more significant in the hydration (~65%) than in the dehydration process (~27%). The slower dehydration kinetics and the lower temperature difference between the heat transfer fluid and bed during dehydration impede HTE in the dehydration process. During the hydration process, the reaction is faster, and heat is generated spontaneously creating a temperature difference of around

200^{0}C across the heat exchanger wall. During the dehydration reaction, however, the difference between the initial thermal equilibrium temperature and the HTF inlet temperature is set at 100^{0}C. The heat transfer is further slowed down by the slower kinetics of the dehydration process compared to the hydration.

4.5 Comparison of the Reactors ‘a’ and ‘b’

We next investigate the influence of fins in the reactor ‘b’ for the hydration process. Time evolution of temperatures and the averaged conversion within the reactor are depicted in Figure 28 with and without fins.

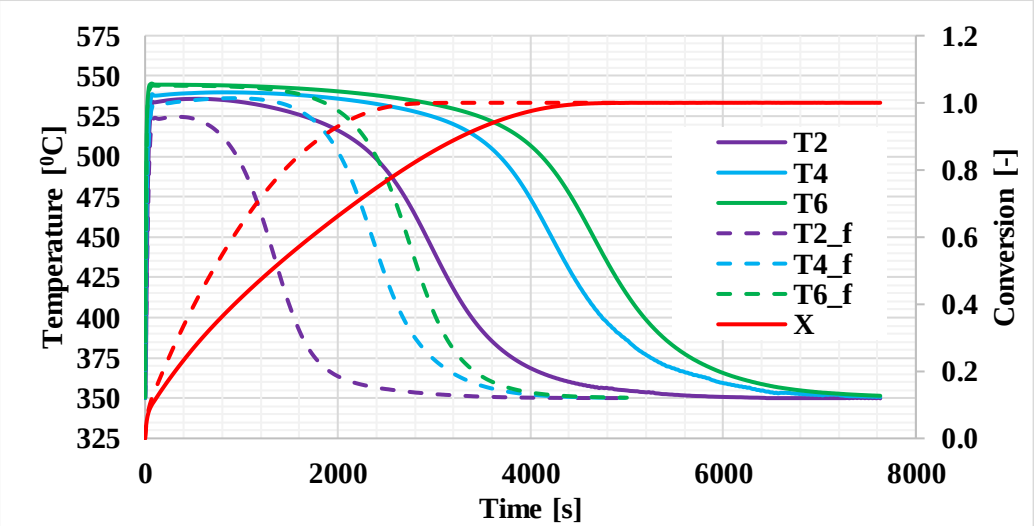

Figure 28. Average conversion and temperature at points 2, 4 and 6 in the reaction bed of the reactor 'b' with fins (dotted lines) and without fins (solid lines) during the hydration process.

The volume of the reaction bed is the same as in the reactor ‘a’. Size of the HTF channel in the reactor ‘b’ is determined in the same way as in the reactor ‘a’ with fixed Reynolds number of 1500 and HTF inlet velocity of 25m/s. Despite the similar dimensions as in the reactor ‘a’ and the same operating conditions, the heat transfer

enhancement with fins is not as profound as in the reactor 'a'. Total conversion time for the hydration process is ~5400s without fins and ~4000s with the fins. These total conversion times are determined from the actual data as the elapsed time when the conversion reaches the unity. Average conversion time is reduced by ~26% in the reactor 'b' whereas it is ~65% in the reactor 'a' with the same reaction bed size. This difference can be attributed to the fact that there is a smaller contact area between the reaction bed and HTF within the reactor 'b'. The contact area is 0.02611 m^2 in the reactor 'a' and 0.01229 m^2 in the reactor 'b'. The difference in percentage decrease in the average conversion (40.4%) is nearly equal to the percentage decrease in the contact area (~47%) of the wall and the reaction bed.

The difference in the effect of fins between the reactor 'a' and the reactor 'b' also is visible in Figures 29 and 30. The instantaneous isotherms during the hydration process with and without fins in the reactor 'a' and 'b' are depicted in Figures 29 and 30 respectively. Figure 29 shows temperature contours at t=1500s for the reactor 'a' with and without fins.

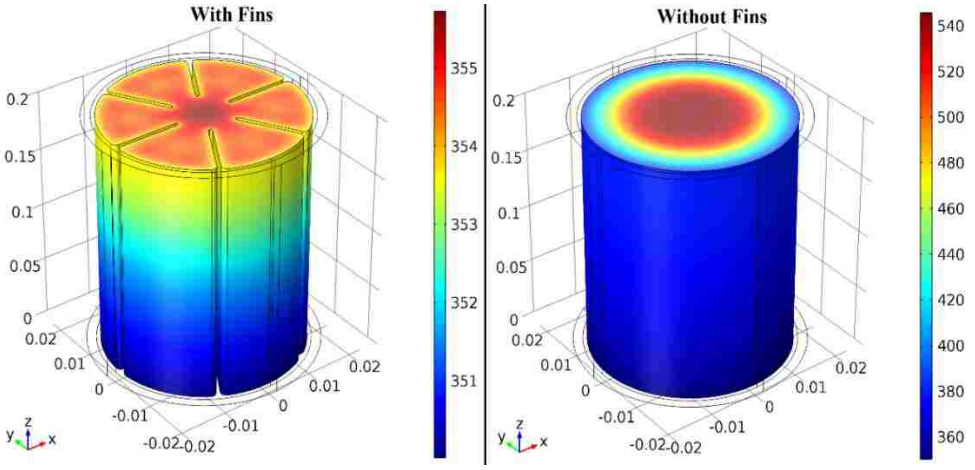

Figure 29. Temperature contours of the reaction bed in the reactor 'a' with fins (left) and without fins (right) at t = 1500s during the hydration process.

It reveals that the reaction bed with fins has almost reached initial thermal equilibrium conditions with removal of the heat. At the same instant, the minimum temperature in the reaction bed without fins on the right is above the initial thermal equilibrium temperature (350^0C) whereas the center of the bed is still close to the maximum reaction equilibrium temperature (550^0C) corresponding to the inlet steam pressure of 2bar.

Figure 30 shows temperature contours of the bed in the reactor 'b' at 2500s during the hydration process. The temperature at the locations between the fins and away from the HTF channel is still close to the 500^0C whereas most of the reaction bed without fins is at a temperature close to the equilibrium temperature (550^0C) corresponding to the inlet steam pressure. Given the effect of fins in the reactor 'a' is far more significant than in the reactor 'b', further simulations were carried out for the different reaction bed sizes of the reactor 'a' for energy release step (hydration) only. The reaction bed sizes of $r_b = 15\ mm$, $r_b = 20\ mm$ and $r_b = 25\ mm$ are considered.

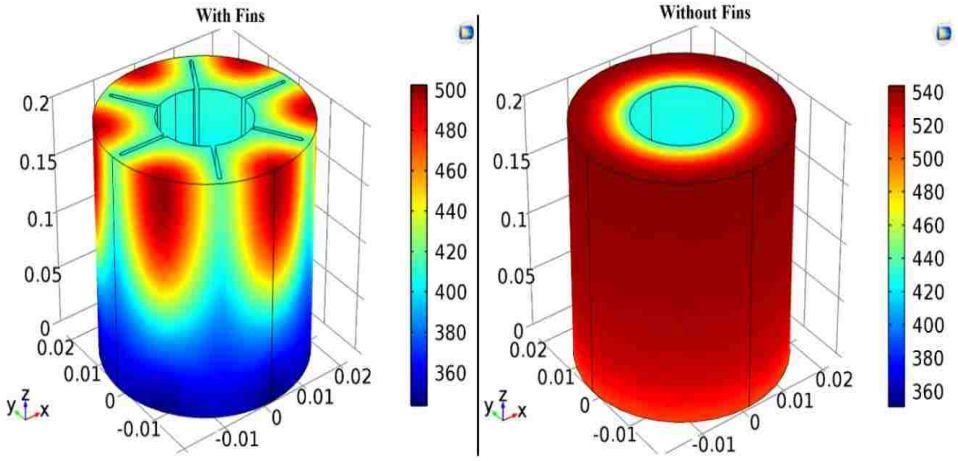

Figure 30 Temperature contours of the reaction bed in the reactor 'b' with fins (left) and without fins (right) at t = 2500s during the hydration process

4.5.1 Reaction Bed Size Variations

The poor thermal conductivity of the solid reaction materials imposes limitations on the diameter of the circular reaction bed whereas the rate of steam transport poses limitations on the height of the bed. The designed HTE significantly overcomes the first limitation provided the bed is heated through outer wall owing to the larger contact area with HTF. The effect of the finned wall is, thus, further investigated by varying the size of the reaction bed with other parameters held unchanged. Figure 31 shows the average conversion during the hydration process for various reaction bed diameters of the reactor 'a' with and without the HTE. The average conversion time is reduced by 73% with HTE for the bed size $r_b = 15\,mm$. As the radius of the reaction bed increases the finned wall becomes increasingly more effective. Average conversion time with HTE is reduced by 77% in case of $r_b = 20\,mm$ and by 80% in case of $r_b = 25\,mm$. Table 3 summarizes the HTE effects in the reactor 'a' for the cases discussed above. The designed fin configuration can effectively overcome the problem of the slower heat transfer rate when the bed size is increased.

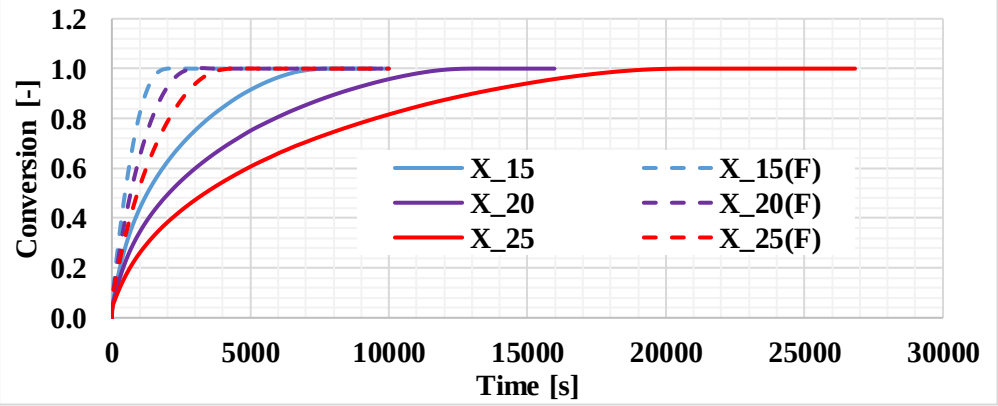

Figure 31. Average conversion for $r_b = 15\,mm, r_b = 20\,mm\ and\ r_b = 25\,mm$ with fins (dashed) and without fins (solid) in the reactor 'a' during the hydration process.

Heat transfer during the charging and discharging process is vital in every TES system. It is particularly more important in TCES as slow rate of heat transport can reverse the reaction in some regions as was observed with the rectangular bed. Figure 32 shows the average temperature profiles for various reaction bed sizes during the hydration reaction. It is obvious that the rate at which heat is removed increases with the proposed HTE. For the reactor 'a' with $r_b = 15\ mm$, the HTE reduce the time to reach initial thermal equilibrium by ~41%. In the same way, the removal of heat from the bed for $r_b = 20\ mm$ and $r_b = 25\ mm$ is completed in ~75% and 77% less time, respectively.

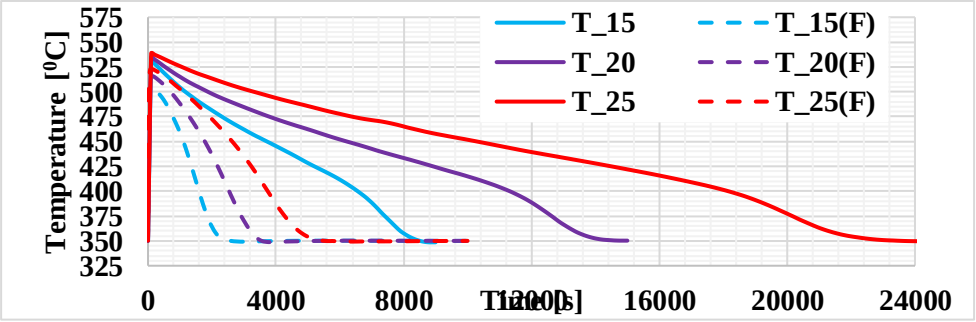

Figure 32. Average bed temperature with fins (dashed) and without fins (solid) during the hydration process for various bed sizes of the reactor 'a'. ($r_b = 15\ mm$, $r_b = 20\ mm$ and $r_b = 25\ mm$)

Table 5 Conversion time for various bed sizes of the reactor 'a' with and without fins

r_b (mm)	v_b (m^3)	Process	Conversion time (s)		% decrease with HTE
			(without HTE)	(With HTE)	
10	2.372e-4	Dehydration	8300	11000	27%
10	2.372e-4	Hydration	4000	1400	65%
15	5.432e-4	Hydration	7500	2000	73%
20	9.757e-4	Hydration	13000	3000	77%
25	1.534e-3	Hydration	20500	4250	80%

4.6 Summary

The reactors with circular reaction beds and two different HTF channel configurations are investigated and compared for the effect of THE. Heat exchanger wall with fins projecting into the solid reaction bed is considered. The vertical fins are arranged radially within the bed with two HTF channel configurations, one with HTF flowing in an outer annular channel (reactor 'a') and other with HTF flowing in a central pipe (reactor 'b'). Charging and discharging processes are simulated in the reactor 'a' with and without HTE. Total conversion time is reduced by ~27% and ~65% for the charging (dehydration) and discharging (hydration) process, respectively. Lesser effect of the HTE in charging process is attributed to the smaller temperature difference between the HTF and the bed and the overall slower dehydration reaction kinetics. HTE is also applied to the reactor 'b' with the same reaction bed size, HTF inlet velocity, and Reynolds number. The reduction in the average conversion during the hydration is found to be 26%. Reduction in the average conversion times increased to 73%, 77% and 80% for the reaction bed radii of 15mm, 20mm, and 25mm, respectively, within the reaction 'a'. The finned reactors introduced here significantly enhance the heat transport to overcome the limitation in size of fixed $Ca(OH)_2/CaO$ reaction bed. It is concluded that to maximize the effect of the HTE the circular reaction bed must be heated from the outer wall. The design of the HTF channel, namely outer annular shell, used in this study is chosen to minimize the computational costs. More efficient and practically feasible way of heating the circular reaction bed through the outer wall, however, is the crossflow configuration between the HTF and the steam flow. This configuration with multiple reaction bed is studied in the next chapter.

CHAPTER 5 REACTORS WITH CROSS-FLOW CONFIGURATION

In this chapter, the reactor with the circular bed is considered with the HTF flowing perpendicular to the bed axis. The reaction gas flows perpendicular to the HTF flow and enters/leaves from the top of the bed. Unlike the configurations studied in the previous chapter with the circular reaction bed, this configuration can be extended to a system of multiple reaction beds with the HTF flowing perpendicular to the beds' axes.

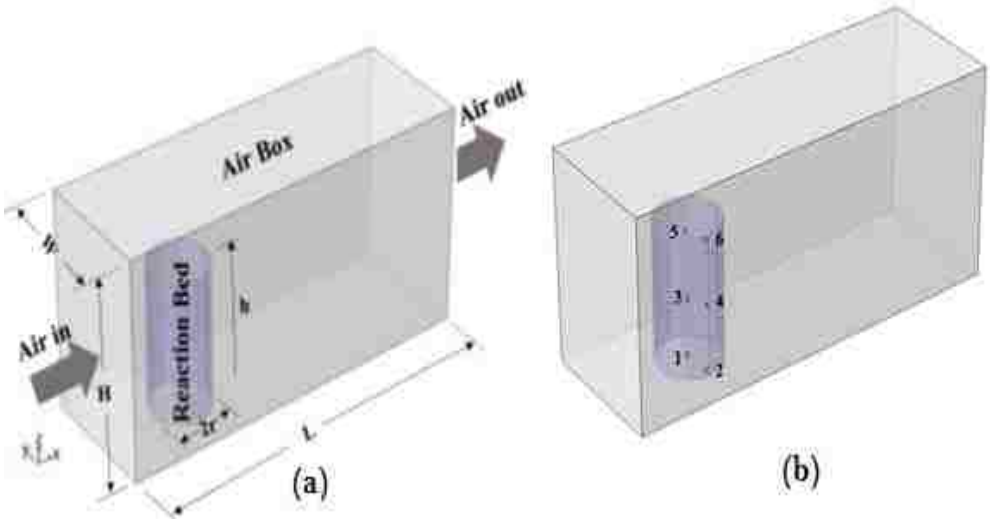

Figure 33. (a) Reference geometry and computational model, and (b) location of the points to record the variables' values.

The reactor configuration is shown in Figure 33 (a). Computational domain consists of the reaction bed and rectangular HTF channel. Size of the HTF channel is chosen to allow enough air volume around the circular bed. Figure 33 (b) shows the location of the points where the temperature and conversion are recorded. Points 1, 3 and 5 are along the bed axis at r = 0. Coordinates of these points are P1(0,0.01h),

P2(0.9r,0.01h), P3(0,0.h/2), P4(0.9r,h/2), P5(0,0.95h), P6(0.9r,0.95h). Dimensions of the bed and the channel are given in Table 6.

Table 6. Dimensions of the reactor in Figure 33.

HTF channel height	H	15 [cm]
HTF channel length	L	30 [cm]
HTF channel width	W	10 [cm]
Reaction bed height	h	10 [cm]
Reaction bed radius	r	10 [mm]
Reynolds number based on HTF channel height	Re	300
Reynolds number based on the diameter of the reactor bed	Re_D	80

Temperature profiles within the bed and average conversion are shown in Figure 34 and Figure 35 for charging and discharging processes respectively. These results correspond to Reynold number Re=300 based on the HTF channel height. The Reynold's number based on the bed diameter is R_{eD}=80. The reaction bed radius is 10 mm. Temperature and conversion profiles at three points along the bed axis are shown. Point 1 is close to the bottom of the bed, point 3 is at the middle, and point 5 is close to the top surface of the bed.

Dehydration proceeds with the heat transfer to the bed. Heat transfer and conversion at point 5 (close to the top face of the bed) is significantly faster than the other locations. This is because the top surface is not insulated and is in contact with HTF. Also during the dehydration process (Figure 34) the steam leaves the bed from the top surface

resulting no significant increase in the bed pressure close to the steam outlet. Consequently, the reaction equilibrium temperature of the bed does not increase and the difference ($T-T_{eq}$) is higher in that region resulting in faster conversion. Similarly, during hydration (Figure 35), the steam enters from the top face of the bed hence resulting in much faster conversion and heat transfer at point 5 than at the lower points.

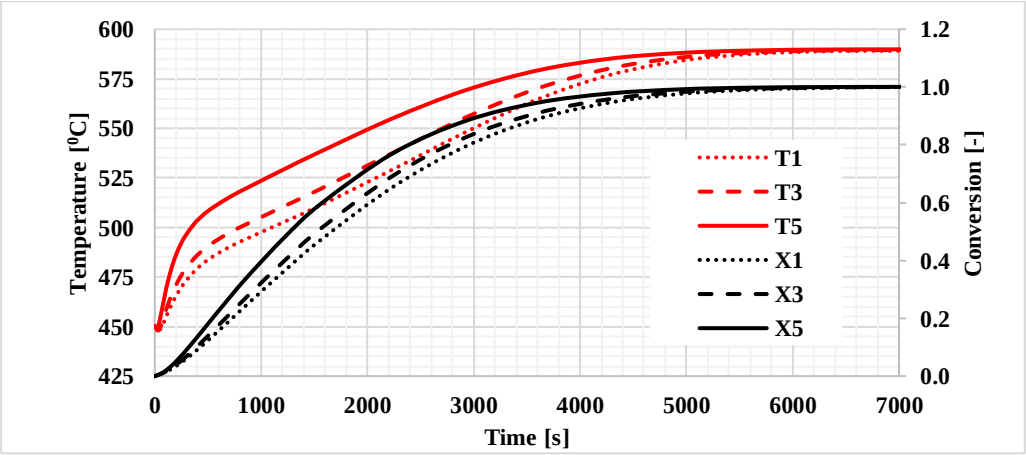

Figure 34. Bed temperatures and conversion during charging process (dehydration process) recorded along bed axis at 0.01h, h/2, and 0.95h.

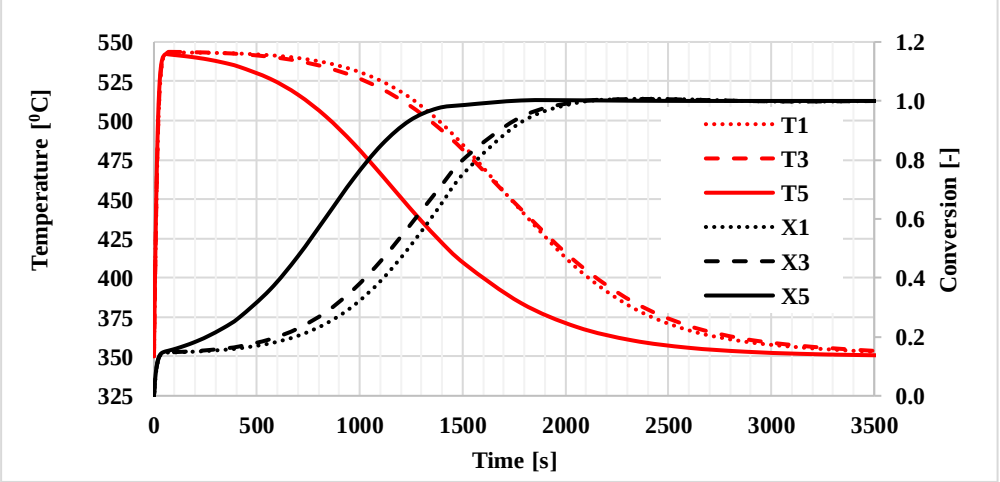

Figure 35. Bed temperatures and conversions during the discharging process (hydration process) along the bed axis at 0.01h, h/2, and 0.95h.

The temperature distribution and conversion are elaborated in more details in Figure 35. Temperature and conversion contours at two instants are shown in five parallel x-y planes along the bed height for hydration process with bed radius of 10 mm. The contours show that heat transfer and conversion are faster at the top surface compared to the other regions as illustrated by the profiles in Figure 34 and Figure 35. Also, the contours are not symmetrical about the bed axis as was observed in a similar bed with outer annular HTF channel in the previous chapter. Another behavior noticeable in the contours shown in Figure 36 is that although the bottom surface is insulated the last part to cool down to the initial temperature is the middle of the bed. This is because despite the insulated bottom of the bed the air flowing past the lower part of the bed is at a lower temperature than the air above it. The top surface is exposed to the HTF at high temperature, but it is also exposed to the HTF from above and from the sides resulting faster heat transfer.

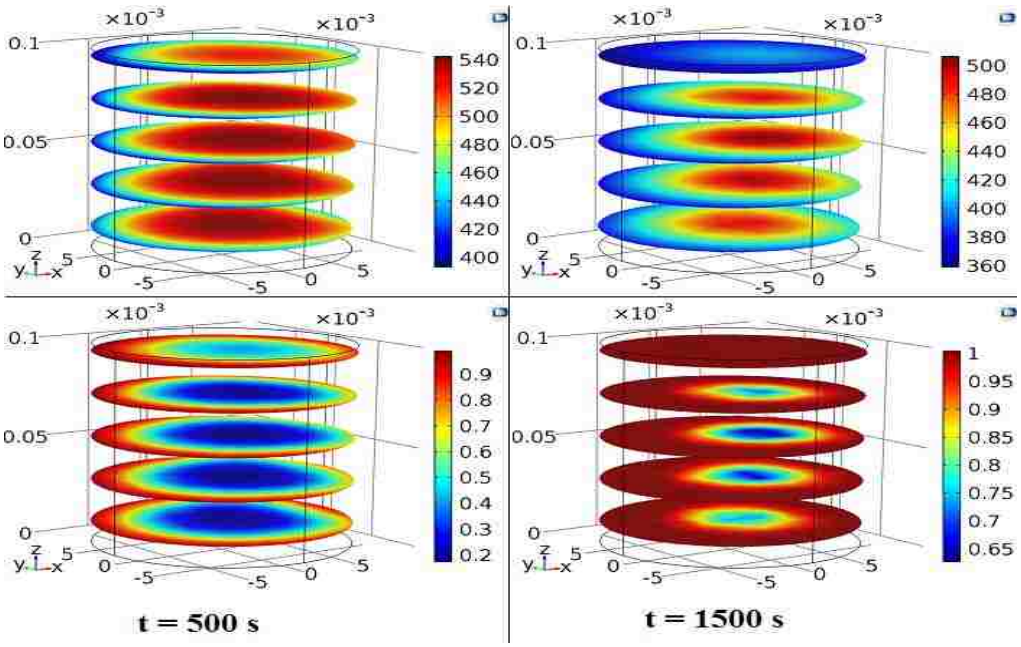

Figure 36. Temperature distribution (above) and the reaction front (bottom) at two instants during the hydration process.

The effect of increasing the bed diameter was studied while keeping Reynolds number constant based on the HTF channel height. Increased bed size will result in an increased Reynolds number around the circular bed. Figure 37 shows the temperature profiles along the bed axis at two points 3 and 5, one close to the top surface and one at the middle. The difference is quite significant when the bed radius is increased from 10mm to 15mm. But the effect of increased Reynolds number is dominant in the earlier stages of the reaction when bed radius is increased from 15mm to 25 mm. The temperature profile T5 close to the top surface for r=25mm has sharper decline after reaching maximum value than that for r=15mm. This is due to higher Reynolds number around the larger bed. However, T5 and T3 for r=25 show rather slow heat transfer in the later part due to poor thermal conductivity within the bed.

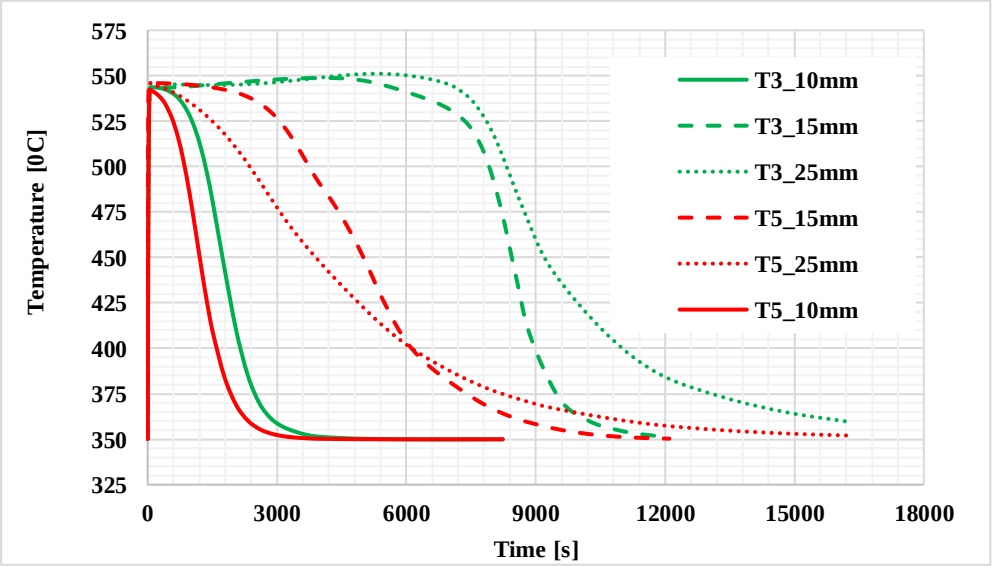

Figure 37. Bed temperatures for various bed sizes (r= 10mm, 15mm and 25mm) during the discharging process (hydration process) at two points along the bed axis at 0.01h, h/2, and 0.9h.

The delayed heat transfer in case of r=15mm and r=25mm also results in a reverse reaction where bed temperature becomes higher than the reaction equilibrium temperature as shown for the conversion profiles at points 3 and 5 in Figure 38. It is observed that the conversion close to the top surface (point 5) for r=25mm is faster than for r=15mm. This shows the influence of the higher Reynolds number at the beginning of the reaction.

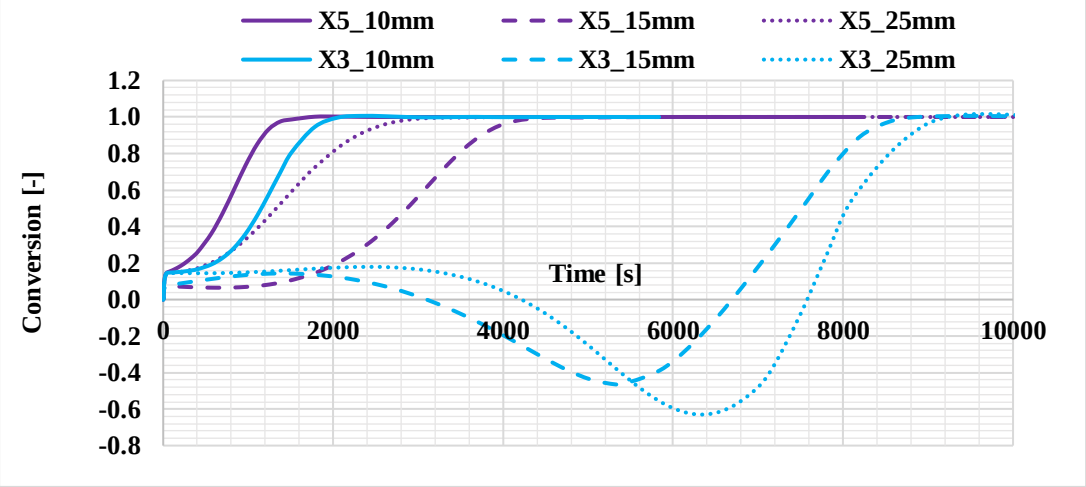

Figure 38. Conversion profiles for various bed sizes (r = 10mm, 15mm and 25mm) during discharging process (hydration process) at two points along the bed axis at 0.01h, h/2, and 0.9h.

Figure 39 shows the reverse reaction at point 3 for a time when the T3 becomes higher than the equilibrium temperature Teq3. This is followed by a sudden increase in the conversion X3 when T3 drops sharply below Teq3.

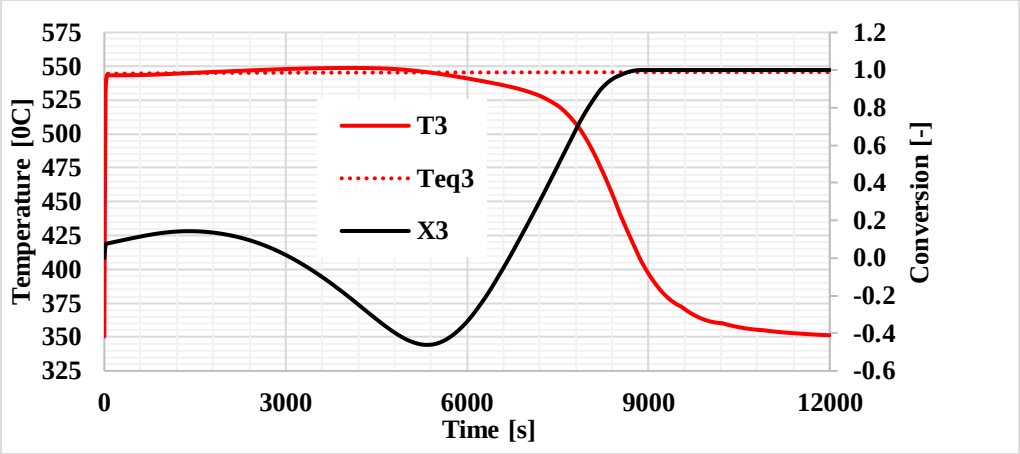

Figure 39. Bed temperature, reaction equilibrium temperature, and conversion at location 3.

To further investigate the effects of varying Reynolds number on the conversion and temperature within the bed hydration process was simulated with the bed radius r=15mm for various Reynolds numbers within the laminar regime of HTF flow. Figure 40 shows the average conversion during hydration for r=15mm at three Reynolds number R_e=100 (R_{eD}=40), R_e=200 (R_{eD}=80) and R_e=400 (R_{eD}=160). The conversion time is reduced with an increase in R_e. The effect can also be seen in Figure 41 where the conversion and temperature profiles at location P3 is plotted as functions of the time.

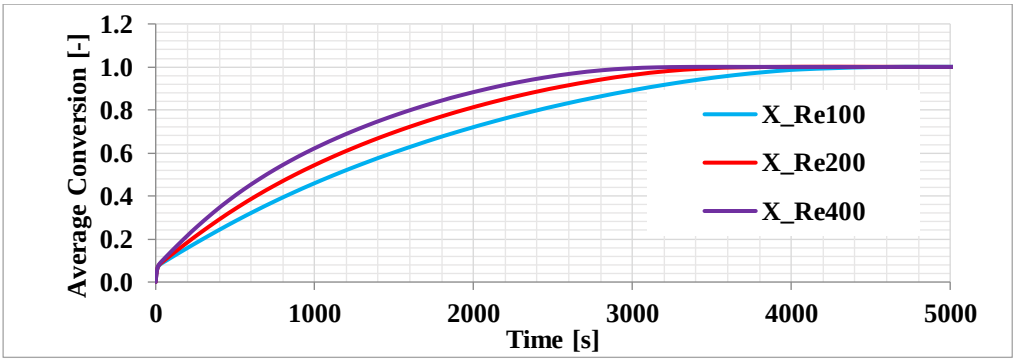

Figure 40. The average conversion as a function of time during the hydration process for the bed porosity for various Reynolds number in laminar regime.

While the reverse reaction can be seen at this central location due to delayed heat transfer, increasing the Reynolds number have a significant effect on individual temperature and conversion profiles as shown in Figure 41.

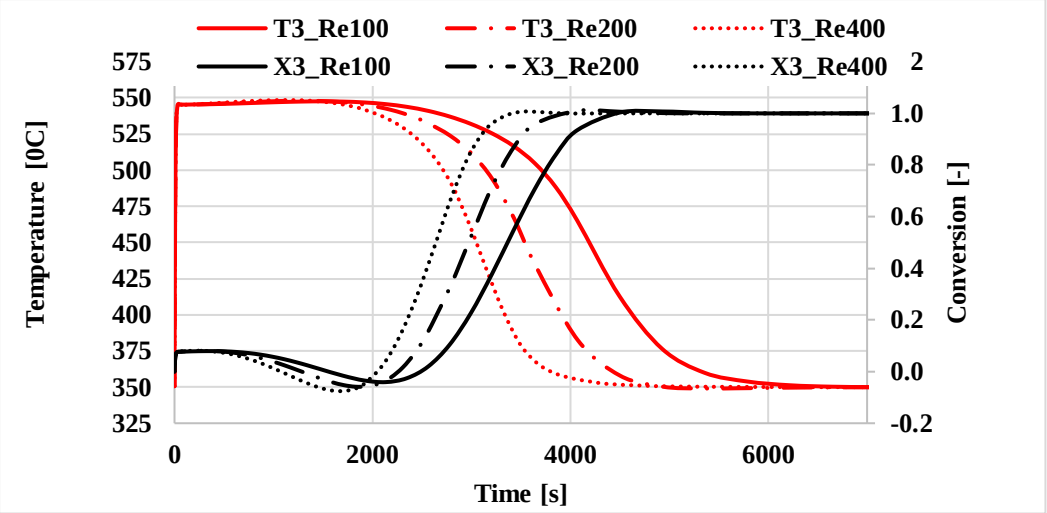

Figure 41 Conversion and temperature profile at point 3 for Re=100,200 and 400.

5.1 Arrays of Reactor Beds

The simulations are carried out using a configuration consisting of an array of reaction beds to exploit the real benefit of using cross-flow configuration. In-line arrangement of the reaction bed is used with laminar flow of the HTF.

Table 7 Geometric and operating parameters for the reactor in Figure 42

HTF channel height	H	20 [cm]
HTF channel length	L	50 [cm]
HTF channel width	W	8 [cm]
Reaction bed height	h	20 [cm]
Reaction bed radius	r	20 [mm]
Reynolds number with respect to HTF channel	Re	200
Reynolds number around the cylindrical bed	Re_D	120

Figure 42(a) shows the arrangement of the reaction beds and flow configuration of the steam and the HTF, and Figure 42(b) shows the location of a probe point in the meddle of each bed where the evolution of temperature, steam pressure and the conversion is recorded during the charging and the discharging processes. Table 7 lists the operating and geometric parameters for the reactor shown in Figure 42. The height of the reaction bed is kept the same as that of the HTF channel. The in-line arrangement is considered with the periodic boundary, as shown in Figure 42.

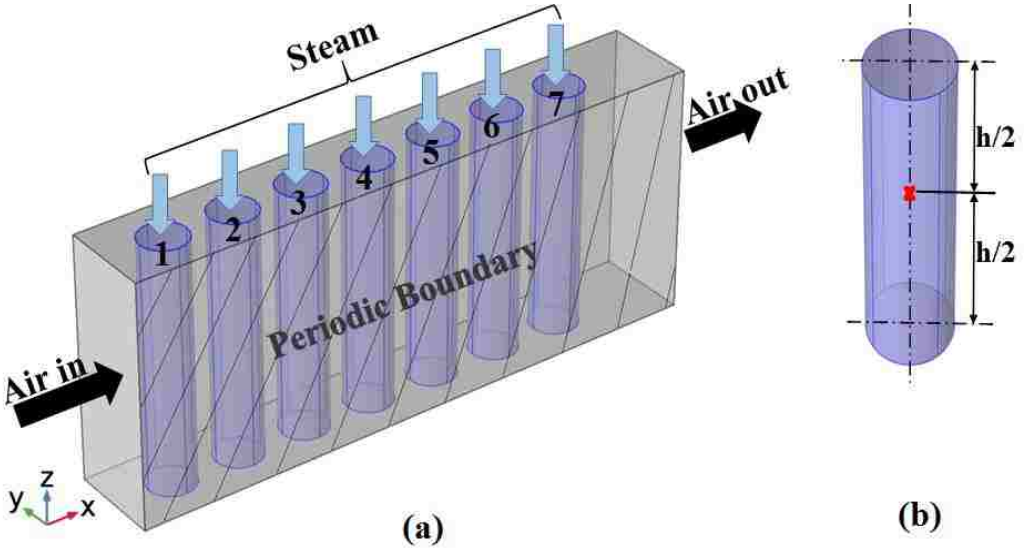

Figure 42. (a) Reactor with multiple beds and cross-flow configuration of the steam and the HTF. (b) Location of the probe point 'P' in the center of each bed to record the variables as a function of time.

5.1.1 Dehydration Process

The average conversion profiles of all the reaction beds, 1-7, for the dehydration (the charging process) are plotted in Figure 43. The conversion in the first bed is completed significantly less time than the second reactor whereas the difference in average conversion time decreases gradually between the two consecutive beds. This

difference becomes almost unnoticeable between the beds 6 and 7 with the average conversion in bed 7 slightly faster than in the bed 6. The last bed in the row, the bed 7, has more convective heat transfer towards the open end of the channel. This is illustrated in the conversion contours at three instants during the dehydration reaction in Figure 43.

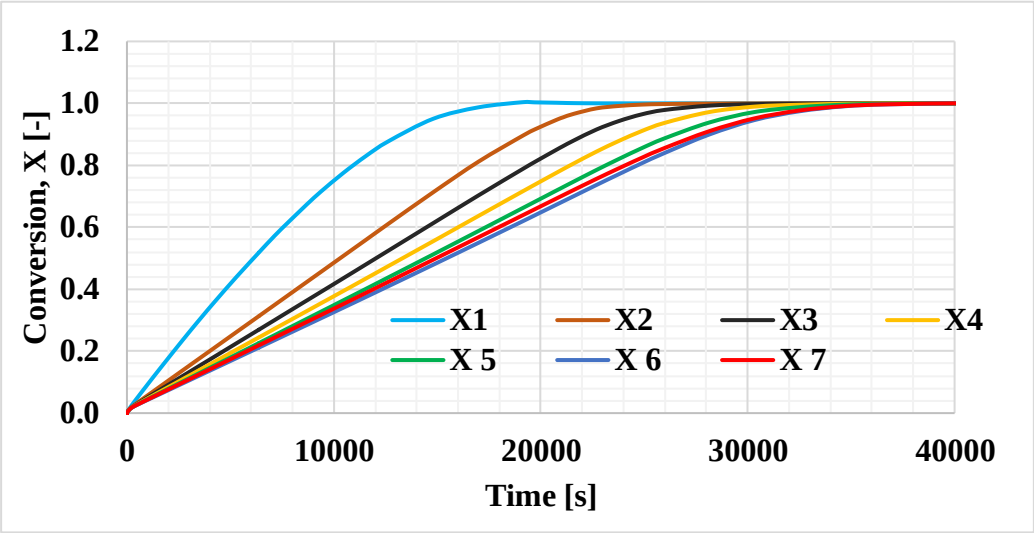

Figure 43. Average conversion in the reaction beds 1 through 7 of Figure 42(a) during the dehydration (charging) process.

The reaction front movement can be seen in Figure 44 in the reaction bed. The contours represent an x-y plane in the middle of the reactor. The shape of the reaction front, as it propagates through each of the reaction bed, is representative of the way heat is being transferred to the bed in this reactor configuration. Also, the faster conversion in the bed 7 than in the bed 6 is visible in the last contour. The temperature difference between the HTF and the beds decreases along the length of the reactor causing slower heat transfer to the bed. This results in the slower conversion rates in the beds towards the downstream of the HTF channel.

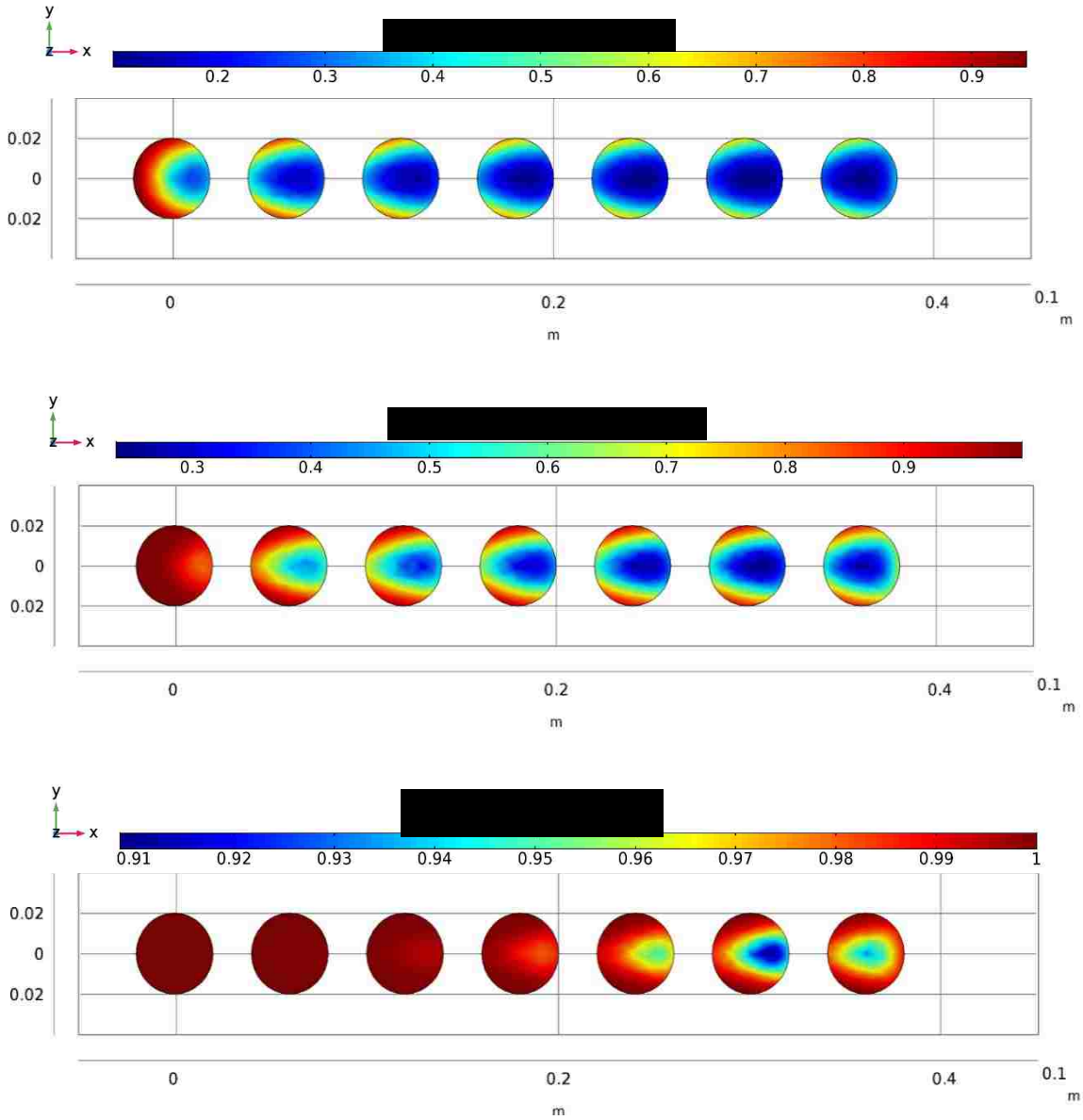

Figure 44. Average conversion at the x-y plane in the middle of the reaction beds at three instants, 8000s, 15000s and 30000s during the dehydration process

The variations in the heat transfer between the HTF and the bed also present along the height of the beds. This is caused by the velocity variations of the HTF between the top and the bottom plates. Figure 45 shows three x-y planes along the bed height at the bottom, in the middle, and at the top (z=0, z=0.1 and z=0.2). The faster heat transfer and conversion in the middle plane is caused by the velocity profile of the HTF flowing

between two parallel top and bottom faces of the HTF channel. The velocity increases towards the center of the plates (top and bottom surfaces) resulting in faster conversion as shown in Figure 45.

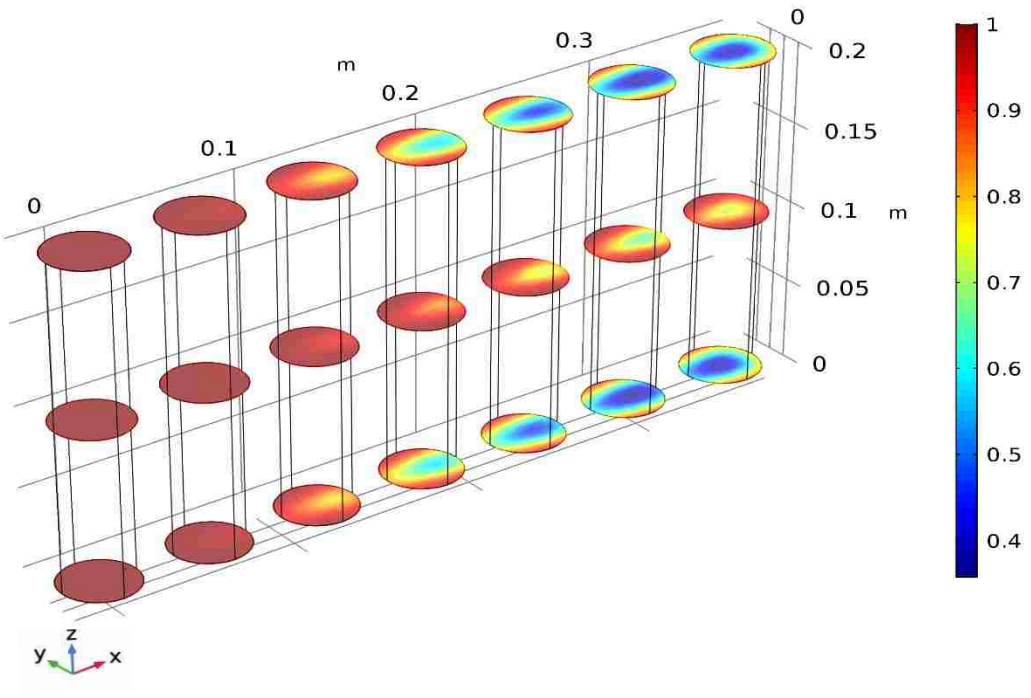

Figure 45. Conversion contours at three x-y planes along the height of the beds.

5.1.2 Hydration Process

The average conversion profiles during the hydration (discharge) process shown in Figure 46 are similar to the dehydration profiles shown in Figure 43. However, there are noticeable differences as well, in addition to the time shift due to the fast kinetics of the hydration reaction.

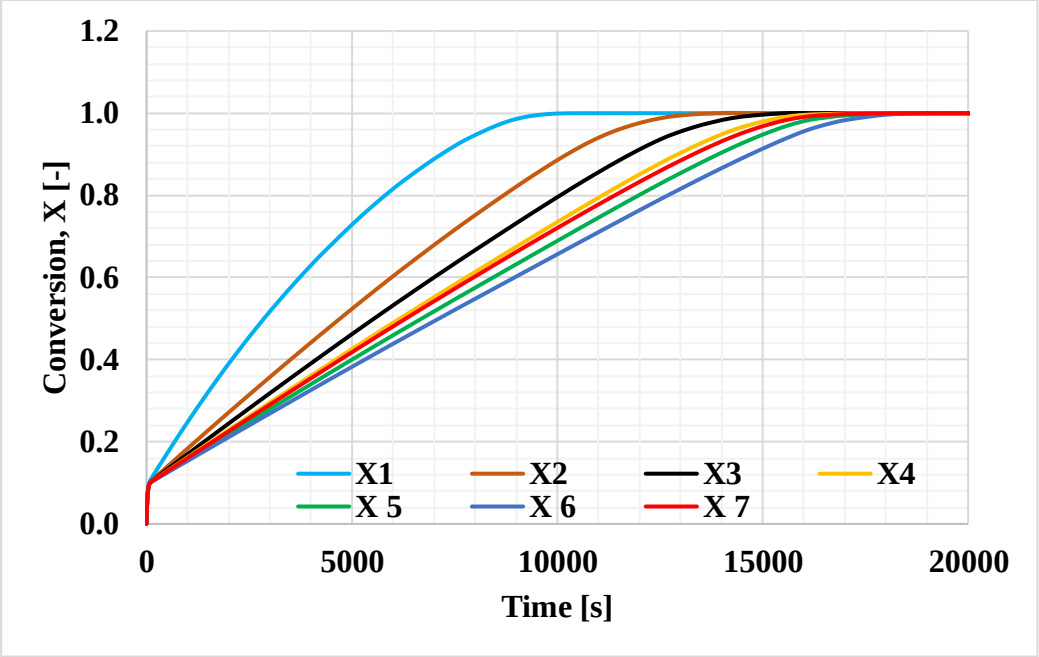

Figure 46. Average conversion in the reaction beds1-7 during the hydration reaction.

The first difference from the dehydration reaction can be noticed at the onset of the hydration reaction. The average conversion in each bed increases spontaneously with the heat release because the initial temperature of the bed is well below the reaction equilibrium temperature. As this difference decreases, the conversion slows down and proceeds with the heat transfer from the bed. Another difference is overserved in the average conversion of the bed 7 which completes before the bed 5 and 6 and almost in the same time as in the bed 4. This is significantly different than the average conversion in the beds towards downstream of the HTF channel during the dehydration process. This can be attributed to an overall faster heat generation within the bed generating a higher temperature difference between the beds and the HTF. Therefore, the convective heat transfer during the hydration reaction has a more profound effect than in the dehydration reaction.

Although the value of average conversion in each bed during the charging and discharging process remains positive at all times, the central regions in the beds experience some reverse reaction due to delayed heat transfer which becomes more significant in the beds towards downstream of the HTF channel. Figure 47 shows the conversion profiles at the point ‘P’, shown in Figure 42(b), in each reactor during the hydration reaction.

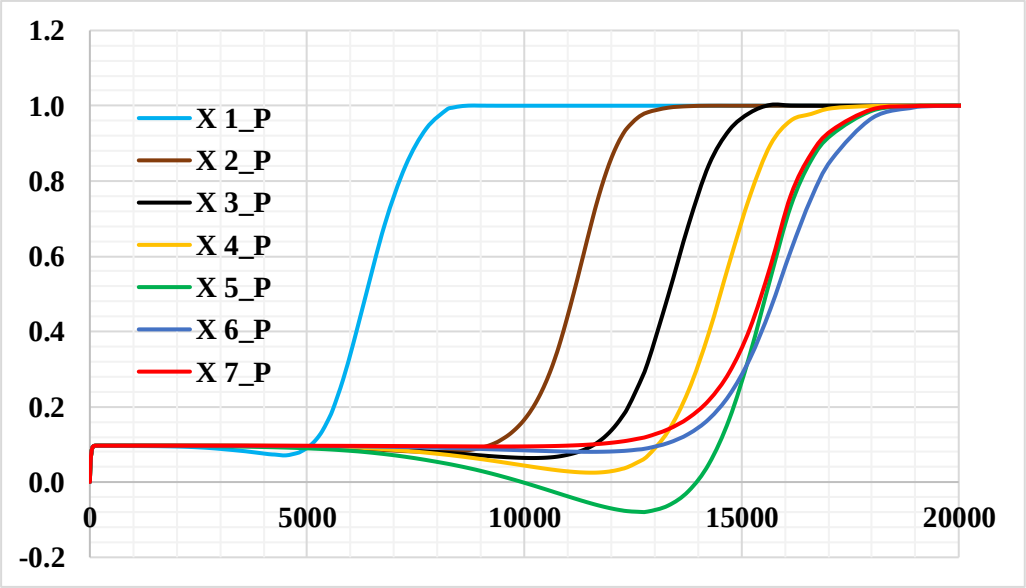

Figure 47. Conversion at point 'P' in the middle of each bed 1through 7 during the hydration process.

It can be seen from Figure 47 that in the central region of each bed the conversion increases instantly at the beginning when the steam is introduced. After the onset of the reaction, however, the beds’ temperatures increase spontaneously and becomes equal to the reaction equilibrium temperature, and there is no conversion in this region for some time as shown by horizontal profiles for each bed. The delayed heat transfer from the middle of the beds with the heat generation within the bed causes the

temperature in this region to go higher than the reaction equilibrium temperature resulting in the reverse reaction in the already converted material. Average conversion time in the bed 5 is the highest in hydration reaction (Figure 46). Therefore, the reverse reaction at the point 'P' in the bed 5 is most significant.

5.2 Summary

A TCES reactor with a single cylindrical bed and an array of cylindrical fixed beds is studied as HTF flows perpendicular to the bed axis. Heat and mass transfer characteristics of the storage system are presented for a single reaction bed. The influence of geometric and operating parameters on the discharging process is examined. The results can be extended to the dehydration as well. Three bed sizes with radii of 10mm, 15mm and 25mm are simulated to study the effect of the poor thermal conductivity of the storage materials. An array of seven in-line reactors, each of 20mm radius, with periodic boundary condition is simulated with cross-flow configuration. The delayed heat transport within the bed for larger bed size and multiple beds results in a reverse reaction. Effect of varying Reynolds number within the laminar flow regime of the HTF is also determined. It is concluded that circular reaction bed indirectly heated by the HTF flowing perpendicular to the bed axis is more advantageous regarding the heat transfer as compared to other configurations investigated in the previous chapters. The problem of lower thermal conductivity could be overcame with the introduction of the heat transfer enhancements studied in the previous chapter. In this way, not only the size of individual reaction bed with circular cross-section can be increased; more reaction beds can be added to the reactor without compromising on its performance and power rating.

CHAPTER 6 CONCLUSIONS

The main objective of this study is to investigate heat and mass transfer characteristics of thermochemical energy storage based on $Ca(OH)_2$ and CaO. A mathematical model is developed to design and investigate the reactors with fixed reaction beds. The coupled set of equations governing heat and mass transport within and to/from the reaction bed(s) along with the reaction kinetics is solved numerically by utilizing a finite element method using COMSOL. The model is used to simulate various reactor configurations regarding the mode of heat transfer between the reaction bed and the HTF channel.

A reactor with a rectangular reaction bed and flat plate heat exchanger is used first to validate the model. Two and three-dimensional analyses of this reactor are performed by varying physical and operating parameters. It is found that a two-dimensional model is a good approximation of the highly porous ($\varepsilon \geq 0.8$) rectangular reaction bed. When the bed porosity is decreased, the steam transport is limited, and the two-dimensional approximation is not valid. Hence, the three-dimensional simulations are carried out for low bed porosities ($\varepsilon < 0.7$). Decreasing the bed porosity increases the energy density of the bed accompanied by the restricted transport of the reaction gas entering or leaving the bed. Lower porosity also results in the slower heat transport within the bed due to the lower thermal conductivity of the reaction materials. Hence, a compromise among these parameters is needed when designing the fixed bed reactor.

Solution to the lower thermal conductivity of the reaction bed with lower porosity is addressed by considering different reactor configurations with circular reaction beds. The circular bed reactors are studied with lower porosity beds ($\varepsilon = 0.5$). The energy

density of the bed can be increased by lowering the bed porosity or by increasing the bed size. The height of the bed is limited by the steam transport. Therefore, in order to get higher energy density without compromising the heat and mass transport during the charging and discharging process is to increase the bed radius instead of the height and to introducing heat transfer enhancements within the bed. The heat transfer can further be enhanced by a proper heat exchange design. Hence, the circular bed reactors are simulated in with various configurations of the HTF channel. In concurrent and countercurrent flow schemes of the steam and the HTF channel, an outer annular HTF channel surrounding the reaction bed is more effective than the internal pipe used as HTF channel.

The wall between the reaction bed and the HTF channel is equipped with fins in case of circular bed reactor to overcome the lower thermal conductivity within the reaction bed. The finned wall becomes more effective with an increase in the size of the bed. The circular bed reactor with the finned wall is investigated for the different bad radii, and the results showed that limitation on the size of the reaction bed can be overcame by including fins.

Despite the effectiveness of the outer annular shell as HTF channel and the introduction of the fins, it is not viable to scale up the circular bed reactor with the HTF flowing parallel to the bed. Therefore, the study is concluded with simulations of the circular bed reactor with HTF flowing perpendicular to the bed axis. This reactor configuration is investigated for a single reaction bed of various radii and also for the multiple beds arranged in line with periodic boundaries at the sides of the HTF channel. Cross-flow of the reaction gas and the HTF flow offers many advantages over all other

configurations using fixed beds. One of the major advantages is that more beds can be added without adding complexity to the system. Walls of the individual beds can be extended into the beds using fins to enhance the heat transfer. Hence, for a gas-solid reaction like this in a fixed reaction bed, the best possible configuration with indirect heat transfer mode is circular reaction bed(s) with cross-flow of the reaction gas and HTF.

6.1 Limitations and Challenges

Value of the Carmen-Kozeny (CK) factor in equation 6 is taken from [48] along with the other properties of the materials. This value is valid for randomly packed bed with a higher porosity used in this study. But it can be misleading to use the same value for a lower porosity bed [63]. It is, therefore, recommended that the CK factor should be carefully determined for reaction material sample being used and the way the bed is packed.

Effective thermal conductivity values of 0.1 for a high porosity bed bed (ε=0.8) to 0.4 for a low porosity bed (ε =0.5) are used [47]. No other sources of documentation for the thermal conductivity of pure $Ca(OH)_2$ and CaO were found. Since the heat transfer is critical in any heat storage system, measurements on thermal conductivities of these solids would help improve the results of the model.

Arrhenius parameters are important in determining the reaction and conversion rates. Wide range of values for these parameters are reported in the literature [57]. Both hydration and dehydration process are strongly dependent on the kinetic model parameters. Hence, it is important to measure these values for the material samples for accurate predictions of the conversion times. Another challenge attached to these

parameters is that these values may slightly differ for the next cycle if any degradation of the materials occurs. Fortunately, stability of $Ca(OH)_2/CaO$ system for 100 cycles have been reported [57] with nearly no changes in the conversion time in a directly heated bed.

A general form of the reaction mechanism is used in equation (20). The pressure term and the function f(X) may vary for different experimental conditions particularly if the particle size used is of higher order (mm or cm). Hence, the reaction mechanism should be determined empirically to for any material sample before using the model to accurately characterize thermochemical storage process. Also, if the particle size increases then porosity variation in the transverse (radial) direction of the bed should be added to the model as well.

The conversion reported in the experiments for this type of reactor is approximately 80% for both hydration and dehydration. Major factors leading to this are channeling and sintering effects. The effect of these is difficult to model because they are the result of experimental conditions. Sintering may be caused by the improper stoichiometric ratio of the reactant gases whereas channeling may occur as the result of reaction gas moving through the powdered bed. Channeling may be reduced by using larger particle size but will be accompanied by other constraints as discussed above.

In conclusion, $Ca(OH)_2/CaO$ reaction system has great potential to be used as short and long-term thermal energy storage at high temperatures. However, more research is needed to overcome the challenges faced by this system as discussed in the preceding paragraphs.

REFERENCES

[1] Dincer, I., Rosen, M. 2002. *Thermal Energy Storage – Systems and Applications*. John Wiley & Son, New York.

[2] Abhay Dinkera, MadhuAgarwala, G.D.Agarwalb, *Heat storage materials, geometry and applications: A review,* Journal of the Energy Institute 90 (2017)1-11

[3] J. Xu, R.Z. Wang, Y. Li. *A review of available technologies for seasonal thermal energy storage.* Solar Energy 103 (2014) 610–638.

[4] S.S. Chandel, Tanya Agarwal. Reviews *Review of current state of research on energy storage, toxicity, health hazards and commercialization of phase changing materials,* Renewable and Sustainable Energy Reviews, 67 (2017) 581-596

[5] Jose Pereira da Cunha, Philip Eames. *Thermal energy storage for low and medium temperature applications using phase change materials – A review,* Applied Energy 177 (2016) 227-238

[6] E. Assis, L. Katsman, G. Ziskind, R. Letan. *Numerical and experimental study of melting in a spherical shell.* International Journal of Heat and Mass Transfer, 50 (2007) 1790–1804.

[7] W. Zhao, S. Neti, A. Oztekin, *Heat transfer analysis of encapsulated phase change material for thermal energy storage.* Applied thermal Engineering, 50(2013)143-151.

[8] P. Pardo, A. Deydier, Z. Anxionnaz-Minvielle, S. Rougé, M. Cabassud, P. Cognet. *A review on high temperature thermochemical heat energy storage.* Renewable and Sustainable Energy Reviews 32(2014)591–610.

[9] Ugo Pelaya, Lingai Luoa, Yilin Fana, Driss Stitoub, Mark Rood. *Thermal energy storage systems for concentrated solar power plants,* Renewable and Sustainable Energy Reviews 79 (2017) 82-100

[10] Guruprasad Alva, Lingkun Liu, Xiang Huang, Guiyin Fang. *Thermal energy storage materials and systems for solar energy applications,* Renewable and Sustainable Energy Reviews 68-1 (2017) 693-706

[11] T. Yan, R. Z. Wang, T. X. Li, L. W. Wang, Ishugah T. Fred. *A review of promising candidate reactions for chemical heat storage.* Renewable and Sustainable Energy Reviews 43(2015)13–31.

[12] Abedin AH, Rosen MA. *A Critical Review of Thermochemical Energy Storage Systems*. The Open Renew Energy J 4 (2011)42–46.

[13] Devrim Aydin, Sean P. Casey, Saffa Riffat. *The latest advancements on thermochemical heat storage systems*. Renewable and Sustainable Energy Reviews 41 (2015) 356–367.

[14] Yate Ding, S.B. Riffat. *Thermochemical energy storage technologies for building applications: a state-of-the-art review.* International Journal of Low-Carbon Technologies, 8 (2013) 106–116

[15] K. Edem N'Tsoukpoe, Hui Liu, Nolwenn Le Pierrès, Lingai Luo. *A review on long-term sorption solar energy storage.* Renew Sustain Energy Rev 13 (2009) 2385-2396

[16] Huili Zhang, Jan Baeyens, Gustavo Cáceres, Jan Degrève, Yongqin Lv. *Thermal energy storage: Recent developments and practical aspects*. Progress in Energy and Combustion Science, 53 (2016) 1-40

[17] N.Yu, R.Z.Wang, L.W.Wang. *Sorption thermal storage for solar energy*. Progress in Energy and Combustion Science, 39 (2013) 489-514

[18] Luisa F. Cabeza a, Aran Sole, Camila Barreneche. *Review on sorption materials and technologies for heat pumps and thermal energy storage*

[19] Prieto C, Cooper P, Fernández AI, Cabeza LF. *Review of technology:Thermochemical energy storage for concentrated solar power plants*. Renew Sustain Energy Rev 60 (2016) 909–929

[20] Jaume Cot-Gores J, Castell A, Cabeza LF. *Thermochemical energy storage and conversion: A-state-of-the-art review of the experimental research under practical conditions*. Renew Sustain Energy Rev 16 (2012) 5207–5224

[21] Medrano M, Gil A, Martorell I, Potau X, Cabeza LF. *State of the art on high-temperature thermal energy storage for power generation. Part 2—Case studies*. Renew Sustain Energy Rev 14 (2010) 56–72

[22] M. Felderhoff, R. Urbanczyk, S. Peil. *Thermochemical Heat Storage for High Temperature Applications – A Review*. Green 3 (2013) 113-123

[23] W.E. Wentworth, E. Chen. *Simple thermal decomposition reactions for storage of solar thermal energy*. Solar Energy 18 (1976) 205–214.

[24] Z.H. Pan, C.Y.Zhao. *Gas–solid thermochemical heat storage reactors for high-temperature applications*. Energy 130 (2017) 155–173.

[25] P. Muthukumar, M. Groll. *Metal hydride based heating and cooling systems: A review*. International Journal of Hydrogen Energy 35 (2010) 3817–3831.

[26] J.M. Criado, M. Macias, A. Macias-Machín. *Analysis of the system CaO-CO2-H2O for storage of solar thermal energy.* Sol Energy, 49 (1992) 83-86

[27] Tescaria, C. Agrafiotisa, S. Breuera, L. de Oliveiraa, M. Neises-von Puttkamera, M. Roeba, C. Sattlera. *Thermochemical solar energy storage via redox oxides: materials and reactor/heat exchanger concepts*. Energy Procedia 49 (2014) 1034 – 1043.

[28] G. Karagiannakis, C.Pagkoura, A. Zygogianni, S. Lorentzou, A. G. Konstandopoulos. *Monolithic ceramic redox materials for thermochemical heat storage applications in CSP plants.* Energy Procedia 49 (2014) 820 – 829.

[29] Keith Lovegrove, Andreas Luzzi, Holger Kreetza. Solar-driven *Amonia based thermochemical energy storage system*. Solar Energy Vol. 67, Nos. 4–6, pp. 309–316, 1999.

[30] Rebecca Dunn, Keith Lovegrove, and Greg Burgess, *A review of Ammonia-based thermochemical energy storage for concentrating solar power*. Proceedings of the IEEE Vol. 100, No. 2, February 2012.

[31] Yukitaka Kato, Norimichi Yamashita, Kei Kobayashi, Yoshio Yoshizawa. *Kinetic study of the hydration of Magnesium oxide for a chemical heat pump*. Applied Thermal Engineering Vol. 16, No. I 1, pp. 853-862, 1996.

[32] Massimiliano Zamengo, Junichi Ryu, Yukitaka Kato. *Magnesium hydroxide – expanded graphite composite pellets for a packed bed reactor chemical heat pump*. Applied Thermal Engineering 61 (2013) 853-858

[33] Y. Kato, J. Nakahata, Y. Yoshizawa. *Durability characteristics of the hydration of magnesium oxide under repetitive reaction*. Journal of Material Science 34 (1999) 475-480.

[34] Guy Ervin. *Solar Heat storage using chemical reactions*. Journal of Solid State Chemistry 22, 51-61 (1977).

[35] P. Pardo, Z. Anxionnaz-Minvielle, S. Rouge, P. Cognet, M. Cabassud. *$Ca(OH)_2/CaO$ reversible reaction in a fluidized bed reactor for thermochemical heat storage*. Solar Energy 107 (2014) 605–616.

[36] Matthias Schmidt1, Marie Gollsch, Franz Giger, Manfred Grün, Marc Linder. *Development of a moving bed pilot plant for thermochemical energy storage with $CaO/Ca(OH)_2$*. AIP Conference Proceedings 1734, 050041 (2016)

[37] S. Álvarez de Migue, J. Gonzalez-Aguilar, M. Romero, *100-Wh Multi-purpose Particle Reactor for Thermochemical Heat Storage in Concentrating Solar Power Plants*. Energy Procedia 49 (2014) 676-683

[38] Yolanda A. Criado, Arthur Huille, Sylvie Rougé, J. Carlos Abanades. *Experimental investigation and model validation of a $CaO/Ca(OH)_2$ fluidized bed reactor for thermochemical energy storage applications*. Chemical Engineering Journal 313 (2017) 1194–1205

[39] S. Fujimoto, E. Bilgen, H. Ogura. *$Ca(OH)_2/CaO$ chemical heat pump system*. Energy Conversion and Management 43 (2002) 947–960.

[40] Michito Kanamori, Hitoki Matsuda, Masanobu Hasatani. *Heat storing/releasing characteristics of chemical heat storage unit of electricity using a $Ca(OH)_2/CaO$ reaction*. Heat Transfer -Japanese Research 25(6)1996.

[41] Hironao Ogura, Rui Shimojyo, Hiroyuki Kage, Yoshizo Matsuno, Arun S. Mujumdar. *Simulation of hydration/dehydration of CaO/Ca(OH)2 chemical heat pump for cold/heat generation*. Drying Technology 17 (1999) 1579-1592.

[42] I. Fujii, K. Tsuchiya, M. Higano, J. Yamada. *Studies of an energy storage by use of the reversible chemical reaction $CaO+H_2O \leftrightarrow Ca(OH)_2$*. Solar Energy Vol. 34, Nos. 4/5, pp. 367–377, 1985.

[43] M.N. Azpiazu, J.M. Morquillas, A. Vazquez. *Heat recovery from a thermal energy storage based on the Ca(OH)2/CaO cycle*. Applied Thermal Engineering 23 (2003) 733–741

[44] Hironao Ogura, Tetsuya Yamamoto, Hiroyuki Kage, Yoshizo Matsuno, Arun S. Mujumdar. *Effects of heat exchange condition on hot air production by a chemical heat pump dryer using $CaO/H_2O/Ca(OH)_2$ reaction*. Chemical Engineering Journal 86 (2002) 3–10.

[45] Hironao Ogura, Mitsutoshi Miyazaki, Hitoki Matsuda, Masanobu Hasatani. *Experimental study on heat transfer enhancement of the solid reactant particle bed in a chemical heat pump using $Ca(OH)_2/CaO$ reaction*. Kagaku Kogaku Ronbunshu 17,916-923(1991).

[46] F. Schaube, A. Kohzer, J. Schutz, A. Wörner, H. Muller-Steinhagen. *De- and rehydration of $Ca(OH)_2$ in a reactor with direct heat transfer for thermo-chemical heat storage. Part A: experimental results*. Chem. Eng. Res. Des. (2013) 856-864.

[47] F. Schaube, Antje Wörner, R. Tamme. *High temperature chemical heat storage for concentrated solar power using gas-solid reactions*. J. Solar Energy Eng. 133 (3) 2011.

[48] Patrick Schmidt, Martin Bouché, Marc Linder, Antje Wörner. *Pilot plant development of high temperature thermochemical heat storage*. The 12th International Conference on Energy Storage, Innostock, 2012.

[49] Matthias Schmidt, Christoph Szczukowski, Christian Roßkopf, Marc Linder, Antje Wörner. *Experimental results of a 10 kW high temperature thermochemical storage reactor based on calcium hydroxide.* Applied Thermal Engineering 62 (2014) 53-559.

[50] M. Linder, M. Schmidt, A. Wörner. *Thermochemical energy storage in kW-scale based /on $CaO/Ca(OH)_2$*. Energy Procedia 49 (2014) 888-897.

[51] Matthias Schmidt, Andrea Gutierrez, Marc Linder. *Thermochemical energy storage with CaO/Ca(OH)2 – Experimental investigation of the thermal capability at low vapor pressures in a lab scale reactor*. Applied Energy 188 (2017) 672–681

[52] Matthias Schmidt, Marc Linder. *Power generation based on the Ca(OH)2/ CaO thermochemical storage system– Experimental investigation of discharge operation modes in lab scale and corresponding conceptual process design.* Applied Energy 203 (2017) 594–607

[53] J. Yan, C.Y. Zhao, *Experimental study of CaO/Ca(OH)2 in a fixed-bed reactor for thermochemical heat storage*. Applied Energy 175 (2016) 277–284

[54] *NIST-JANAF tables*, American Chemical Society, 1998.

[55] Barin and Ihsan. *Thermochemical data of pure substances*. 2nd Edition. Weinheim , Federal Republic of Germany; New York: VCH, 1993.

[56] H. Shao, T. Nagel, C. Roßkopf, M. Linder, A. Wörner, O.Kolditz. *Non-equilibrium thermochemical heat storage in porous media: Part 2- A 1D computational model for a calcium hydroxide system*. Energy 60(2013) 271-282.

[57] F. Schaube, L. Koch, A. Wörner, H. Muller-Steinhagen. *A thermodynamic and kinetic study of the de- and rehydration of $Ca(OH)_2$ at high H_2O partial pressure for thermo-chemical heat storage*. Thermochim. Acta 538 (2012) 9-20.

[58] Dun Chen, Xiang Gao, David Dollimore. *The application of non-isothermal methods of kinetic analysis to the decomposition of calcium hydroxide*. Thermochimica Acta, 215 (1993) 65-82.

[59] M. Khachani, A. El Hamidi, M. Halim, S. Arsalane. *Non-isothermal kinetic and thermodynamic studies of the dehydroxylation process of synthetic calcium hydroxide $Ca(OH)_2$*, J. Mater. Environ. Sci. 5 (2) (2014) 615-624.

[60] Hitoki Matsuda, Takashi Ishizu, Soo Kag Lee, Masanobu Hasatani, *Kinetic study of $Ca(OH)_2$/CaO reversible thermochemical reaction for thermal energy storage by means of chemical reaction*. Industrial and Engineering Chemistry Research., 2014, 53 (32), pp 12594–12601.

[61] P.E. Halstead and A.E. Moore, *The Thermal Dissociation of Culcium Hydroxide*. J. Chem. Soc. (1957)3873-3875.

[62] J. A. C. Samms, B. E. Evans. *Thermal dissociation of $Ca(OH)_2$ at elevated pressures*. J. Appl. Chem. 1968, 18, 5−8

[63] Francisco J. Valdes-Parada , J. Alberto Ochoa-Tapia, Jose Alvarez-Ramirez. *Validity of the permeability Carman–Kozeny equation: A volume averaging approach.* Physica A 388 (2009) 789–798.

Vita

Qasim Ranjha was born on May 5, 1983 in a rural area of Punjab province, Pakistan. He did his undergraduate degree in Mechanical Engineering (2004) and masters in Thermal Power Engineering (2010) from University of Engineering and Technology Lahore, Pakistan. He then started teaching undergraduate courses in a sub-campus of the same university in 2006.

He won the Fulbright scholar for his Ph.D. in 2013. He took study leave from his teaching job and joined Mechanical Engineering department.at Lehigh University in Fall 2013. At Lehigh University, he joined Dr. Alparslan Oztekin's research group and did research on thermal energy storage with emphasis on solar thermochemical storage. He successfully defended his dissertation on the design of thermochemical storage reactor on May 3rd, 2018. He will resume his teaching job at University of Engineering and Technology after completing his Ph.D.